Bulk and Surface Modifications for Achieving Highly Efficient Perovskite-Silicon Tandem Solar Cells

submitted to

Indian Institute of Science Education and Research Pune in partial fulfilment of the requirements for the BS-MS Dual Degree Programme

by

Swayam Basu

Indian Institute of Science Education and Research Pune

Dr. Homi Bhabha Road,

Pashan, Pune 411008, INDIA.

March 2025

Supervisors: Prof. Jozef Poortmans and Dr. Yinghuan Kuang

Certificate

This is to certify that this dissertation entitled Bulk and Surface Modifications for Achieving >30% Perovskite Silicon Tandem Solar Cells towards the partial fulfilment of the BS-MS dual degree programme at the Indian Institute of Science Education and Research, Pune represents study/work carried out by Swayam Basu at EnergyVille Lab, IMEC Genk under the supervision of Prof. Jozef Poortmans, Department of Electrical Engineering (ESAT),KU Leuven and Dr. Yinghuan Kuang, R&D Project Leader (IMEC), during the academic year 2024-25.

Supervisors:

Jozef Poortmans

Yinghuan Kuang

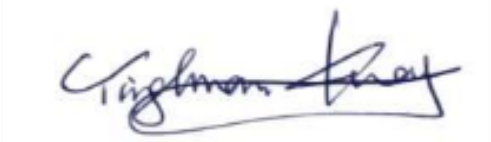

Declaration

I hereby declare that the matter embodied in the report entitled “Bulk and Surface Modifications for Achieving Highly Efficient Perovskite-Silicon Tandem Solar Cells” are the results of the work carried out by me at the Department of Physics, Indian Institute of Science Education & Research (IISER) Pune, under the supervision of Prof. Jozef Poortmans and Dr. Yinghuan Kuang, and the same has not been submitted elsewhere for any other degree. Wherever others contribute, every effort is made to indicate this clearly, with due reference to the literature and acknowledgement of collaborative research and discussions.

Swayam Basu (20201094)

This thesis is dedicated to

Mumma and Baba

Abstract

The efficiency of perovskite-silicon tandem solar cells has rapidly increased in recent years, yet challenges in material stability, defect passivation, and scalability remain barriers to commercialization. This thesis explores bulk and surface passivation strategies alongside scalable deposition techniques to enhance the performance of 1.67 eV wide-bandgap perovskite solar cells suitable for tandem integration. The fabrication was carried out using a hybrid deposition approach, where the perovskite absorber was formed via co-evaporation of inorganic precursors followed by solution-based organic cation deposition. A 1:0.1 PbI_2:CsBr co-evaporation ratio, found to provide better conformality on textured silicon substrates in another study, was adopted, ensuring alignment with tandem device requirements.

In the initial phase, spin-coating was used to evaluate bulk and surface passivation strategies for 1.67 eV perovskite films. 2,3,4,5,6-Pentafluorobenzyl phosphonic acid (pFBPA) was tested as a bulk additive, but its effects on film crystallinity and device performance required further study. In terms of surface passivation, pFBPA, Piperazinium Iodide (PI), and Propane-1,3-Diammonium Iodide ($PDAI_2$) were investigated, with trends in V_{oc} enhancement but reductions in other performance parameters, ultimately lowering device efficiency. Additionally, for PI, a rinsing step was introduced to assess its impact on passivation effectiveness. However, batch-to-batch variability in spin-coated devices led to a transition to blade-coating, a more scalable deposition method offering improved film uniformity and process control.

With blade-coating, the perovskite precursor concentration was optimized to achieve the highest possible efficiency for the baseline device. 0.41 M was identified as the most effective concentration. Additionally, to maintain the 1.67 eV bandgap, the organohalide concentration ratio was adjusted during blade-coating, ensuring bandgap consistency across samples. MACl, which was included in the precursor solution during spin-coating, was further investigated under blade-coating, where it was found to enhance crystallinity, increase grain size, and passivate defects, leading to longer charge carrier lifetimes. Solvent engineering for blade-coating was explored, comparing isopropanol (IPA) with and without N-methyl pyrrolidone (NMP) additions. 1% NMP initially improved device performance, but prolonged illumination studies revealed ion migration effects, leading to bandgap shifts and stability concerns. $PDAI_2$ was revisited for blade-coated surface passivation. Higher concentrations led to insulating effects, while lower concentrations showed incomplete coverage. A rinsing step was introduced, which mitigated unwanted film aggregation and improved device performance. These results highlight the importance of precise control over passivation strategies, deposition conditions, and solvent selection in optimizing perovskite films for tandem integration. The study provides key insights into defect mitigation, scalable processing, and film stability, laying the groundwork for further advancements in high-efficiency, industrially viable perovskite-silicon tandem solar cells.

Contents

Chapter 1: Introduction **1**

1.1 Climate Change and the Role of Photovoltaics……..... 1
1.2 Basic Working Principles of Solar Cells……..... 2
1.3 Performance Quantifiers……..……..... 3
1.4 Silicon Solar Cells ……..……... 5
1.5 Shockley-Queisser Limit ……..... 6
1.6 Multi-Junction Solar Cells……. 6
1.7 Thin-Film Solar Cells……..... 7
1.8 Perovskite – Crystal Structure and Properties …….…… 9
1.9 Wide Bandgap Perovskites for Tandem Applications……..... 10

Chapter 2: Perovskite Layer Development **12**

2.1 A Brief Overview of the State of the Art for Wide-Bandgap Perovskites…… 12
2.2 Perovskite Synthesis Methods…….…. 13
2.2.1 One-Step Deposition……. 14
2.2.2 Two-Step Hybrid Deposition……. 14
2.3 Perovskite Single Junction Cell Fabrication……. 15
2.3.1 Hole Transport Layer……. 16
2.3.2 Self-Assembled Monolayer (SAM)……... 17
2.3.3 Perovskite Deposition…… …… 19
2.3.3.1 Co-Evaporation……... 19
2.3.3.2 Spin-Coating……... 19
2.3.3.3 Blade-Coating……. 20
2.3.4 Electron Transport Layer……... 21
2.3.5 Metal Contact……. 21
2.4 Characterization Techniques……. 22
2.4.1 Solar Simulator……. 22
2.4.2 Photoluminescence (PL) Spectroscopy……. 23
2.4.3 Scanning Electron Microscopy (SEM)……. 24

Chapter 3: Bulk and Surface Defect Passivation **25**

3.1 Spin-coating…… 25
3.1.1 Reference Recipe……. 25
3.1.2 Bulk Modification…… 26
3.1.2.1 pFBPA……... 27

3.1.3 Surface Modification……..... 30
3.1.3.1 pFBPA……..... 31
3.1.3.2 PI…… 34
3.1.3.3 $PDAI_2$…… 36
3.1.4 Problems with Spin-coating…… 37
3.2 Optimizing Blade-coating Baseline…… 38
3.3 Investigating MACl Effects…… 44
3.4 Solvent Selection…… 47
3.5 Blade-coated perovskite surface passivation……. 51
3.5.1 Surface Passivation with PDAI2…… 51

Chapter 4: Conclusion and Outlook **58**
Acknowledgements **62**
Bibliography **63**

Chapter 1: Introduction

1.1 Climate Change and the Photovoltaics Emergence

Climate change remains a critical global issue, with rising temperatures and extreme weather events posing significant risks to ecosystems and human societies. The International Renewable Energy Agency (IRENA) reports that renewable energy, particularly solar power, is essential for achieving the goals set by the Paris Agreement. In 2023, solar energy was the largest source of renewable capacity at 36.7% or 1418 GW, followed by 32.7% hydropower (1265 GW), 26.3% wind energy (1017 GW), 3.9% bioenergy (149 GW) and traces of geothermal and marine energy, as per the IRENA report, represented in Fig 1.1. The combination of technological advancements, economies of scale, lower material costs, policy support, and fierce market competition has led to declining costs of solar modules, which have dropped by over 80% since 2010, and thus have made solar energy one of the most cost-effective solutions for reducing greenhouse gas emissions while meeting the growing global energy demand [1].

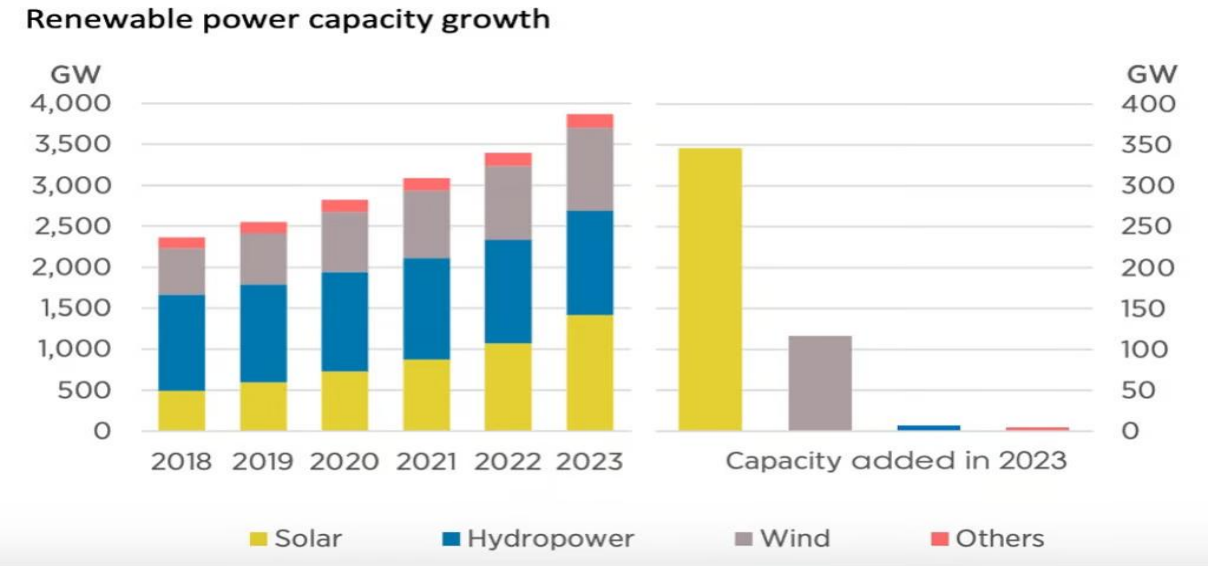

Fig 1.1: Cumulative renewable power capacity until 2023 and capacity added in 2023
Source: IRENA 2023 Report [1]

To limit global warming to 1.5°C, the International Energy Agency (IEA) estimates that annual solar PV installations must increase to at least 1 terawatt (TW) by 2030, up from approximately 250 GW installed in 2023 [2]. This rapid expansion requires innovation and investment in next-generation solar technologies like tandem solar cells, which offer higher efficiencies by capturing a broader spectrum of sunlight. According to a report by the Fraunhofer Institute, tandem cells have the potential to exceed 40% efficiency under laboratory conditions, compared to the current 29.4% efficiency limit of single-junction silicon cells [3]. Scaling up the deployment of such advanced technologies is essential for achieving the 75 TW of PV capacity projected to be required by 2050 to meet global energy needs sustainably [2].

1.2 Solar Cell - Basic Working Principles

Solar cells, also known as photovoltaic (PV) cells, convert sunlight into electricity by using a semiconductor material to generate and direct charge carriers through an internal electric field.

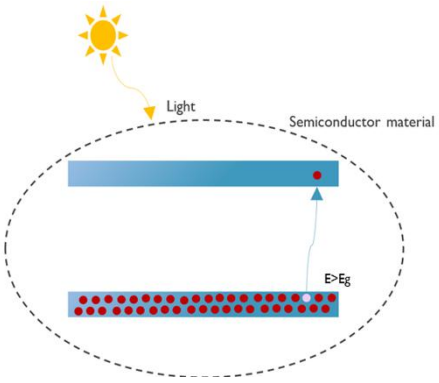

Fig 1.2: Representation of Photovoltaic Effect

Solar cells work on the principle of photovoltaic effect, the physical mechanism by which a substance produces an electric current when exposed to light [4]. It happens when photons hit a semiconductor material, like silicon, and excite electrons from the valence band to the conduction band by transferring their energy to them as shown in Fig 1.2. As a result, electron-hole pairs are formed, and the built-in electric field of the p-n junction drives the electrons toward the n-type side

(which has an excess of electrons) and the holes toward the p-type side (which has an excess of holes).

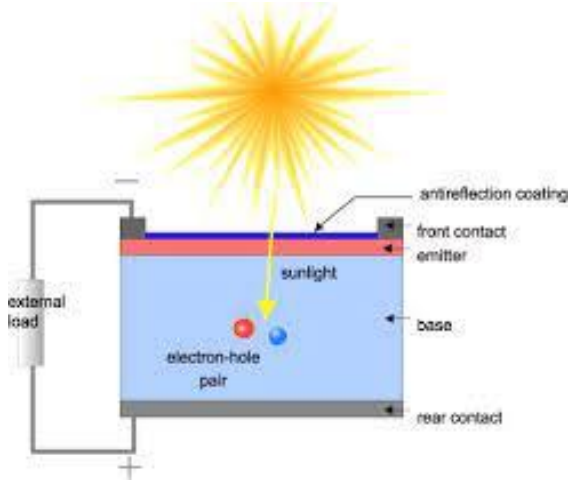

Fig 1.3: Basic Solar Cell Structure, PVE Education

Producing electricity using a solar cell consists of 3 major steps: light absorption, generation/separation of carrier charges, and transport and extraction of carrier charges to finally produce current [4]. Consequently, choosing the appropriate band gap material for proper light absorption is necessary. For the p-n junction (in Silicon solar cells) which helps in charge separation, different types of p and n semiconductors are used. Whereas in perovskite solar cells, to help transport and extract the charges (electrons and holes) transport materials are incorporated in solar cells: Electron Transport Material (ETM) for electron extraction and Hole Transport Material (HTM) for hole extraction [4]. Thus, the basic structure of a solar cell is illustrated in Fig 1.3.

1.3 Performance Quantifiers

The following section gives a brief description of some of the most commonly used parameters used to assess the performance of a solar cell.

The open-circuit voltage (V_{oc}) represents the maximum voltage when no current flows, largely influenced by recombination losses and material properties [5]. The open-circuit voltage

corresponds to the amount of forward bias on the solar cell due to the bias of the solar cell junction with the light-generated current. A higher V_{oc} is indicative of a larger bandgap and is directly related to the separation of quasi Fermi levels of the conduction and valence bands under illumination [5].

The short-circuit current (Isc) is defined as the photocurrent generated under standard illumination, governed by light absorption and charge carrier collection efficiency [6]. It is the amount of current a solar cell (under illumination) produces when the external circuit is shorted or the circuit voltage is equal to 0. Since solar cells with larger active areas generate more charge carriers on illumination leading to higher Isc, this parameter is not suitable to compare solar cells with different active areas [6]. Hence, short-circuit current density (Jsc) is used as it normalizes Isc to the device area and allows for accurate and fair comparisons.

$$Jsc = \frac{Isc}{Area} \tag{1.1}$$

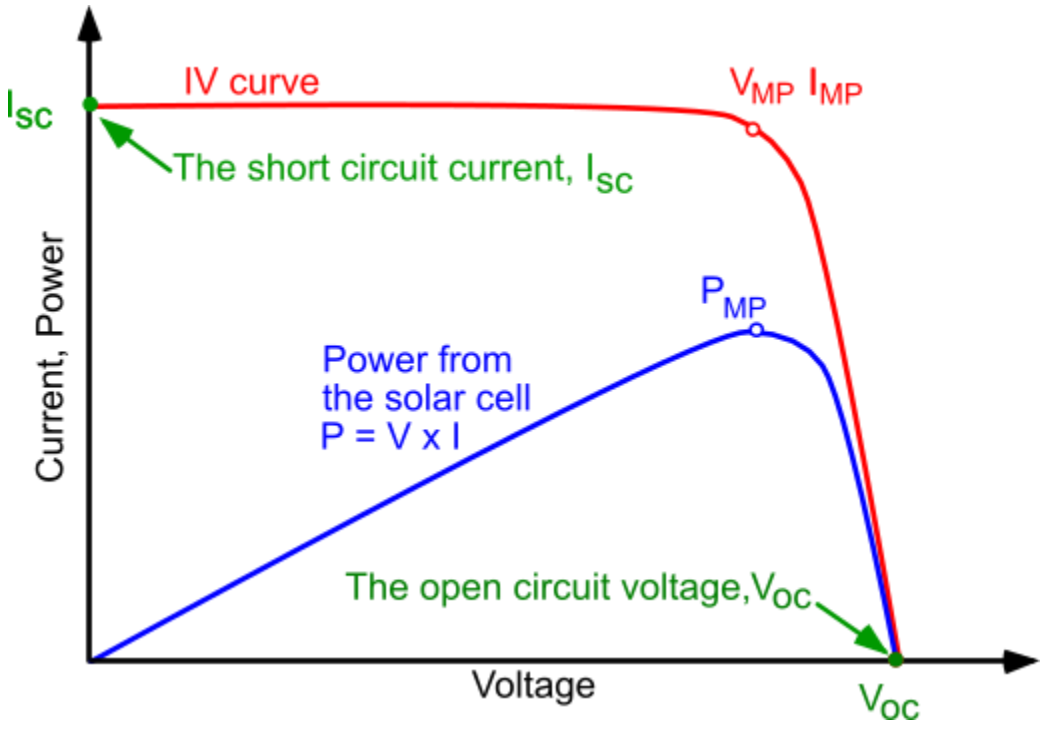

Fig 1.4: PV, IV Curves; PVE Education

Maximum Power Point (MPP) is the operating point at which the solar cells produce its highest power output [7]. From the PV Curve as plotted in Fig 1.4, we can find the voltage at the MPP or V_{MPP} and the current at the MPP or I_{MPP}.

$$P_{MPP} = V_{MPP} \, . \, I_{MPP} \tag{1.2}$$

The Fill Factor (FF), calculated as the ratio of maximum power output to the product of V_{oc} and Jsc, provides insight into the quality of the diode characteristics and resistive losses. Graphically, the FF is a measure of the "squareness" of the solar cell [8].

$$FF = \frac{P_{MPP}}{Voc.Isc} \tag{1.3}$$

Power Conversion Efficiency (PCE) is defined as the ratio of output electrical power to incident solar power, indicating how effectively the cell converts sunlight into electricity [9].

$$PCE = \frac{P_{out}}{P_{in}} \text{ X } 100\% \tag{1.4}$$

These quantifiers collectively determine the effectiveness of a solar cell and guide improvements in material selection, device architecture, and processing techniques.

1.4 Silicon Solar Cells

Due to their high efficiency, low material cost, long term stability and mature manufacturing ecosystem, silicon solar cells are presently the most widely used solar cells. To make a basic Silicon solar cell, a high purity Silicon wafer undergoes a doping process, to form a p-n junction. The p-type doping is obtained by introducing atoms of group III elements; with respect to Si, they have one valence electron less, which allows a positive charge behaviour; the elements most commonly used are boron and gallium. The n-type is obtained by introducing elements of group V, because they have one valence electron more than Si, providing an extra electron and giving a negative charge behaviour. Front side metallic contacts, (usually silver fingers) help collect and

transport charge carriers while a rear metallic contact completes the circuit. An anti-reflection coating (such as SiN_x or TiO_2) can be used to help improve the amount of light entering the cell.

1.5 Shockley Queisser Limit

When charge carriers are generated under illumination, there are several loss mechanisms that can limit the efficiency of the solar cell. These include radiative recombination where excited electrons and holes can recombine before they are extracted to an external circuit. The electrons come down to the valence band and combine with the hole thus losing their energy in form of a radiated photon with energy equal to the bandgap. Another loss mechanism is thermalization where photons with energy higher than the bandgap are utilized but the excess energy gets lost as heat [10]. In 1961, Shockley and Queisser calculated the theoretical efficiency limit of a single-junction solar cell, considering fundamental loss mechanisms such as sub-bandgap transmission losses, thermalization of excess photon energy, and radiative recombination. They estimated a maximum efficiency of ~30% for a 1.1 eV bandgap silicon cell [10]. However, real-world devices suffer from additional losses—including non-radiative recombination (defect states), reflection losses, and resistive losses—which further reduce practical efficiency [10]. Presently, the highest recorded efficiency for silicon solar cells is 27.3% from LONGI Solar (depicted in Fig 1.6). Thus, there is a necessity to look for alternatives to help overcome this SQ limit.

1.6 Multi-junction solar cells

One effective approach to surpassing the Shockley-Queisser (SQ) limit is by layering multiple solar cells, with each cell designed to efficiently capture a specific portion of the solar spectrum. This allows for broader absorption and conversion of sunlight compared to single-junction cells. The wide bandgap cell can absorb the higher energy photons, so it is positioned as the first cell that the incident light encounters. If the energy is lower than the bandgap of this cell, it is transferred to the cell below, which has a lower bandgap and is able to absorb photons with longer wavelengths, and so on until the last cell in the stack. By leveraging this design, tandem and multi-junction solar cells exceed the efficiency constraints of single-junction devices [11]. This

technology remains one of the most well-researched and has the potential to be a commercially viable advancement in photovoltaics.

1.7 Thin Film Solar Cells

Silicon is an indirect bandgap material which means the minimum energy level of the conduction band and the maximum energy level of the valence band are at different points in momentum space. As shown in Fig 1.5 a), the transition of an electron from the valence band to the conduction band requires not only the absorption of a photon to provide the necessary energy, but also the involvement of a phonon to conserve momentum. This makes the absorption coefficient of such materials lower requiring thicker material to absorb sufficient sunlight for efficient energy conversion [12].

However, for direct bandgap materials, photons can excite electrons from the valence band to the conduction band without requiring phonon assistance as shown in Fig 1.5 b). Thus, having higher absorption coefficients, most of the sunlight is absorbed within just a few hundred nanometers (~300-800 nm) of material, making a thin-film structure feasible [12].

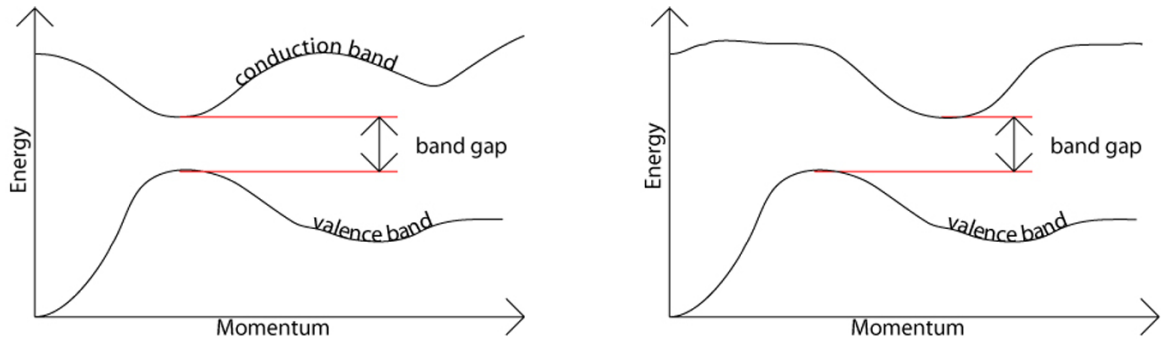

(a) Direct bandgap (b) Indirect bandgap

Fig 1.5: Direct and Indirect bandgap as represented in an E-k diagram [12]

III-V semiconductors, particularly gallium arsenide (GaAs), possess a direct bandgap, making them highly efficient for solar cells and various optical applications. However, despite their

exceptional performance, the high production costs restrict their use mainly to specialized fields such as space technology [12].

While crystalline silicon remains the dominant material in the solar industry, thin-film solar cells are gradually gaining traction due to ongoing research and development. Unlike conventional silicon-based cells, which require thick wafers, thin-film technologies utilize photon-absorbing layers that are only a few microns or even submicron in thickness. These ultra-thin layers can be deposited onto flexible substrates, enabling lightweight and adaptable solar solutions. This approach not only reduces material consumption but also offers potential cost savings and new applications. Key materials in thin-film solar technology include cadmium telluride (CdTe), copper indium gallium selenide (CIGS), and halide perovskites. As shown in Fig 1.6 the record efficiency for perovskite cells rose from 14.1 % in 2013, achieved by EPFL, to 26.7 % in August 2024, set by USTC. In the silicon-perovskite tandem field, the current highest efficiency is held by Longi, a 34.6% record cell [13].

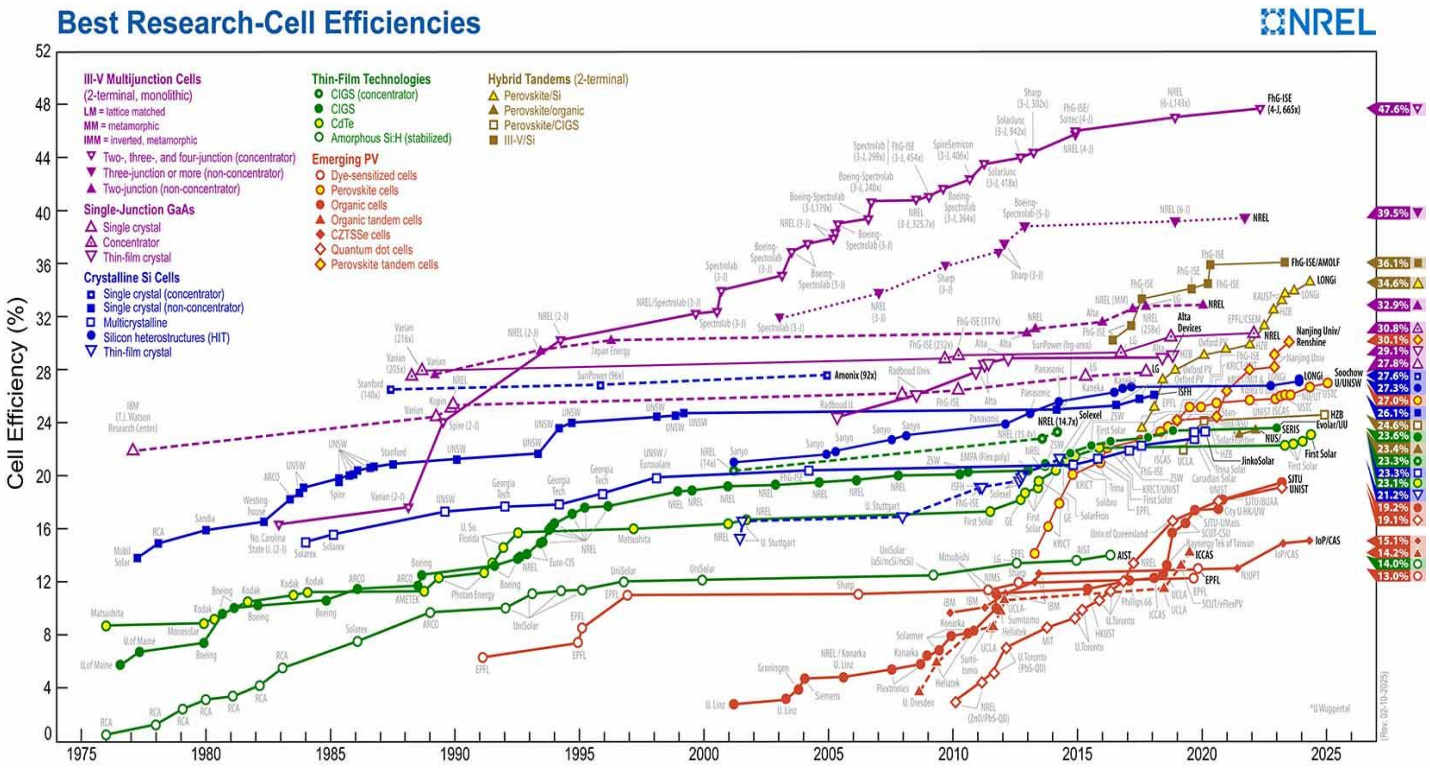

Fig 1.6: Best Research-Cell Efficiency Chart, from NREL [13]

1.8 Perovskite – Crystal Structure and Properties

The perovskite crystal structure (ABX_3) consists of two cations, A and B, and an anion, X. The A-site cation, which can be either organic or inorganic, is relatively larger, while the B-site cation is typically a smaller inorganic metal. The X-site anion is usually a halogen or oxygen, completing the structure.

Within its tetragonal unit cell, the A cation is centrally located, while the B cations form corner-sharing octahedra, with X anions positioned along the edges. When viewed as an assembly of cubic polyhedra, the unit cell can be described as an A cation surrounded by eight B-centered octahedra, where X anions occupy the vertices of these octahedra [14]. This distinctive arrangement is key to the electronic and optical properties that make perovskites highly efficient in applications like solar cells [14].

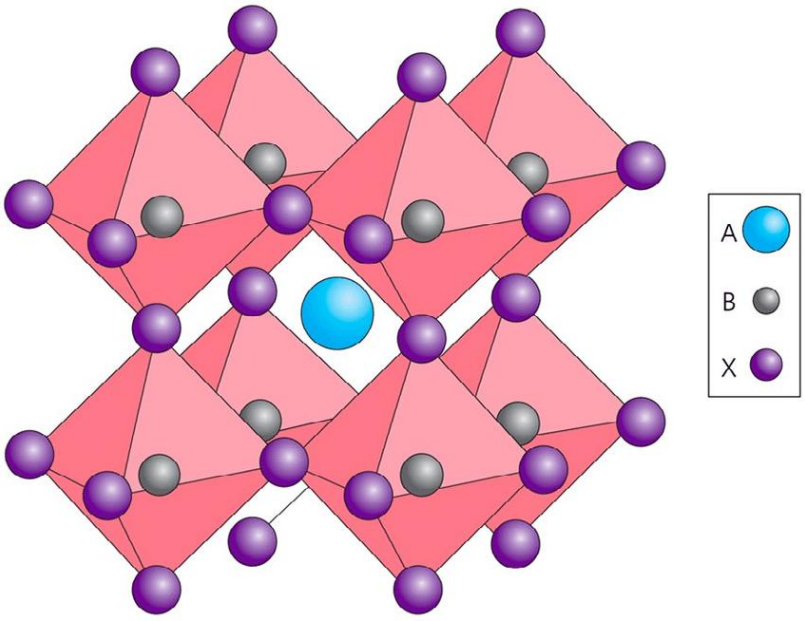

Fig 1.7: Perovskite Crystal Structure [15]

The perovskite unit cell offers remarkable compositional flexibility, as a wide range of elements can occupy each lattice site. Specifically, around 24 elements have been identified for the A-site, 50 for the B-site, while the X-site can be occupied by halides, oxygen, or thiocyanate (SCN). This

extensive variability contributes to the diverse structural configurations observed within the halide perovskite family [14].

If the A-site cation is too small relative to the B-site cation, the structure may deviate from the ideal cubic arrangement, resulting in tetragonal or orthorhombic phase transitions. Additionally, perovskites allow for cation mixing, where multiple elements can simultaneously occupy the A-site or different oxidation states of the same element can coexist, enabling precise compositional tuning. In perovskite solar cell research, the most extensively studied materials are hybrid organic-inorganic metal halides, which have shown great potential for high-efficiency photovoltaic applications[14]. These complex compounds generally feature A-site cations like methylammonium ($CH_3NH_3^+$), formamidinium ($CH(NH_2)_2^+$), or cesium (Cs^+). The B-site is typically occupied by a post-transition metal, such as lead (Pb^{2+}) or tin (Sn^{2+}). The X-site consists of a halide anion, commonly bromine (Br^-), chlorine (Cl^-), or iodine (I^-) [14].

1.9 Wide Bandgap Perovskites

Wide-bandgap (WBG) perovskites, typically classified as those with a bandgap exceeding or around 1.7 eV, have become a crucial component in next-generation photovoltaics, particularly in tandem solar cells, semitransparent photovoltaics, and indoor energy harvesting applications[15]. Unlike conventional perovskites, which are optimized for single-junction devices, WBG perovskites are tailored to maximize energy absorption in tandem configurations by efficiently utilizing high-energy photons while transmitting lower-energy photons to the bottom sub-cell [15].

The bandgap of WBG perovskites is primarily engineered by tuning the halide composition (e.g., adjusting the iodide-to-bromide ratio) and modifying the A-site cations (e.g., incorporating Cs^+, FA^+, or MA^+) [15]. While these modifications enhance optical properties and enable better spectral matching for tandem devices, they also introduce several challenges. One of the most critical issues is halide phase segregation, where iodide- and bromide-rich domains form under continuous illumination. This phenomenon leads to bandgap inhomogeneity, causing localized defects and performance degradation over time [15] . Additionally, WBG perovskites tend to suffer from higher voltage losses (V_{oc} deficit) due to non-radiative recombination, interfacial charge

accumulation, and increased defect density (especially deep level traps introduced by higher bromide content) compared to their lower-bandgap counterparts[15]. Despite these challenges, WBG perovskites remain crucial for high-efficiency tandem solar cells, particularly in perovskite-silicon tandems, where the perovskite top cell typically requires a bandgap of 1.7–1.9 eV to maximize efficiency [15]. Recent research has shown that achieving stable and efficient WBG perovskites necessitates careful halide composition tuning to minimize phase segregation, defect passivation using molecular additives, and controlled crystallization strategies [15]. Moreover, processing techniques such as co-evaporation and blade coating are being explored to enhance film uniformity and reproducibility, addressing the fabrication challenges associated with these materials [15].

The continued development of WBG perovskites is crucial for advancing tandem photovoltaics, with ongoing efforts focused on improving stability, reducing recombination losses, and optimizing deposition techniques to achieve commercially viable, scalable, and high-performance solar cells.

Chapter 2: Perovskite Layer Development

2.1 State of the Art for WBG Perovskites: A Brief Overview

As mentioned earlier, to increase the bandgap of WBG Perovskites, using Bromine to partially replace Iodine in the X positions of the perovskite crystal. As shown in Fig 2.1, we can see how bandgap can be tuned using different compositions. Requiring a bandgap around 1.7 eV, inorganic $CsPbI_3$ fits the bill as it has a bandgap of roughly 1.73 eV. However, it was found to be structurally unstable as the phase transforms spontaneously from a photoactive α-phase at high temperature to a photoinactive δ-phase when cooling down to room temperature [17]. Mixed halide perovskites with high Br ratios face the Hoke effect, where photo-induced phase segregation to I-rich and Br-rich domains increases, leading to reduction in attainable V_{oc} and device instability under illumination [18].

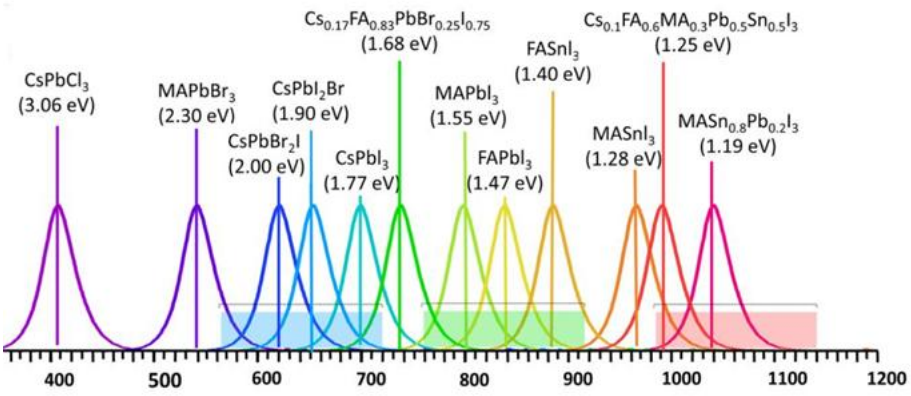

Fig 2.1: Perovskite bandgap tunability as a function of composition [43]

Thus, composition engineering becomes paramount. To improve photostability, Cesium(Cs) mixed with Formadinium($HC(NH_2)_2$ (FA) or Methylammonium (CH3NH3) (MA) helps along with a slight increase in bandgap [19]. Snaith et al. utilized a combination of FA and Cs as A-site

cations to mitigate phase segregation and minimize energetic disorder in a 1.74 eV $FA_{0.83}Cs_{0.17}Pb(Br_{0.4}I_{0.6})_3$ perovskite. This approach demonstrated improved stability compared to single A-cation counterparts, such as $FAPb(Br_{0.4}I_{0.6})_3$ and $MAPb(I_{0.6}Br_{0.4})_3$ perovskites [20]. Bush, McGehee, and their team investigated the effect of varying the Cs content in $Cs_xFA_{1-x}Pb(Br_\gamma I_{1-\gamma})_3$ perovskites. Their findings indicated that increasing the Cs ratio in the A-site cations, rather than raising the Br content in the halide anions, is a more effective strategy for widening the bandgap while simultaneously enhancing V_{oc} without compromising photostability [21].

Apart from changing the crystal composition, interface engineering is also an important aspect to help improve the wide bandgap properties, cutting down the V_{oc} deficit and improving stability. In p-i-n configuration where the Hole Transport Layer (HTL) is stacked before the perovskite, the buried interface lies between the HTL and perovskite and selecting an appropriate HTL or an HTL-perovskite interface helps control perovskite crystal nucleation and growth. Self-assembled monolayers (SAMs) such as Me-[4-(9H-carbazol-9-yl)butyl]phosphonic acid (Me-4PACz) [22], 2PACz and MeO-2PACz [23], and their combinations (e.g., Me-4PACz/2PACz [24] and MeO-2PACz/Me-4PACz [25] mixtures), as well as (4-(7H-dibenzo[c,g]carbazol-7-yl)butyl)phosphonic acid (4PADCB) [26] and MeO-4PADCB [27], are commonly used as hole transport layers in high-performance perovskite solar cells. Additionally, the interface between perovskite and C60, a commonly used electron-selective transport layer in inverted p-i-n perovskite solar cells, plays a crucial role. Effective passivation of perovskite surface defects helps minimize recombination at this interface. Molecules such as 2,3,4,5,6-pentafluorobenzylphosphonic acid (pFBPA), Propane-1,3-diammonium iodide (PDAI2) and Piperazinium iodide (PI) help passivate traps at the ETL-perovskite interface and lead to better energy alignment.

2.2 Different Perovskite Synthesis

Perovskite synthesis methods can be broadly classified based on the number of steps in which the precursors are deposited. The two most common approaches are one-step deposition, where all precursors are introduced simultaneously, and two-step deposition, where the perovskite is formed sequentially through an intermediate phase.

2.2.1 One Step Deposition

In the one-step process, perovskite is formed by directly depositing a precursor solution using various techniques such as blade-coating, spray-coating, and spin-coating. For large-area, scalable fabrication, blade-coating and slot-die coating are preferred, often combined with gas or vacuum-assisted quenching. The film thickness depends on the precursor concentration, coating speed, and the gap between the substrate and the blade or slot-die [31]. Post-deposition annealing is typically necessary.

2.2.2 Two-Step (Hybrid) Deposition

In the two-step process, the lead halide layer is first deposited using solution-based methods such as spin-coating, blade-coating, or slot-die coating, or via vacuum deposition. The organohalide solution is then deposited through either solution or vacuum processing. Various techniques, including precursor additives, solvent annealing, and surface modifications, can be used to enhance the quality of the perovskite films.

In this approach, the inorganic precursors (such as PbI_2 and CsBr) are first thermally co-evaporated to form a structured inorganic scaffold, ensuring conformal coverage on complex surfaces. This is followed by spin-coating or blade-coating an organic halide solution (e.g., FAI/FABr in ethanol), which infiltrates the scaffold and reacts with the inorganic components during annealing to form a perovskite layer[45]. This method allows for better control over film morphology and composition, leading to improved optoelectronic properties[45]. The structured inorganic scaffold provides a stable template for the subsequent organic infiltration, reducing pinholes and enhancing uniformity, making it particularly suitable for high-efficiency perovskite-silicon tandem solar cells [45].

In this project, the two-step deposition or hybrid deposition was used with co evaporation followed by spin-coating or blade-coating. The different deposition processes used in the fabrication of these perovskite solar cells are explained in the subsequent sections.

2.3 Fabrication of Perovskite Single Junction Cells

Silicon bottom cells are more delicate and expensive compared to glass substrates due to their fragility and higher production expenses. Although the objective is to develop tandem solar cells, initial research is typically conducted on glass substrates to optimize perovskite solar cells before transitioning to silicon.

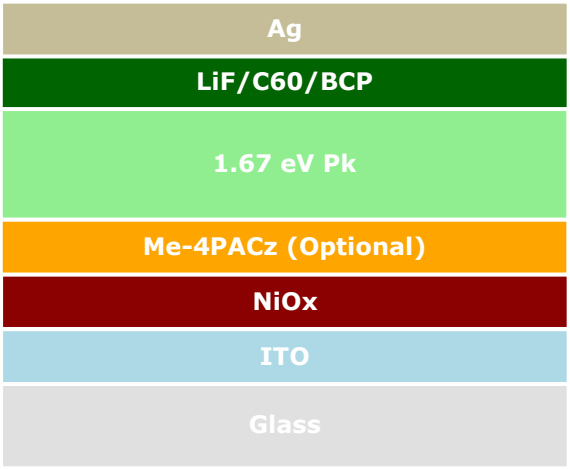

Fig 2.2: Solar Cell Stack

Fig 2.2 shows the basic structure of our inverted p-i-n perovskite solar cell. The single-junction solar cells fabricated for this study are based on 3x3 cm glass substrates with patterned ITO. For each substrate, 12 cells with an active area of 0.125 cm^2 are made.

The first step involves rigorous cleaning of the ITO substrates. The substrate is initially scrubbed with water and soap, then soaked in a soap solution and cleaned in an ultrasonic bath for 10 minutes. This is followed by 10-minute sonication in deionized water, acetone and isopropanol respectively. After drying the substrates, the different charge transport layers are deposited.

The charge transport layers, Hole Transport Layer (HTL) and Electron Transport Layer (ETL), play a crucial role in facilitating charge extraction and minimizing recombination losses in perovskite solar cells. These layers help establish a built-in electric field that drives electrons

toward the ETL and holes toward the HTL, ensuring efficient charge separation. Additionally, they serve as selective contacts, allowing only the desired charge carriers to pass while blocking the opposite type, thereby reducing charge accumulation and recombination. Effective energy level alignment between the perovskite and the transport layers is essential for optimizing charge transfer, as a well-matched band structure minimizes energy barriers, enhances carrier injection, and improves overall device performance.

2.3.1 Hole Transport Layer

In the p-i-n configuration (shown in Fig. 2.2), the hole transport layer (HTL) serves as the first layer deposited on the transparent conductive oxide (TCO). In this study, indium tin oxide (ITO) is used as the TCO. The HTL acts as the substrate for deposition of the perovskite layer, making its material selection crucial, as it directly affects the perovskite morphology. Beyond facilitating hole transport and blocking electrons, the HTL also improves interface quality by reducing defect states [31].

Various hole transport layers (HTLs) are used, including both organic and inorganic materials. Among inorganic HTLs, metal oxides are a common choice due to their chemical stability, high transmittance, scalability, and low cost. However, surface defects pose a challenge.

For p-i-n perovskite solar cells, NiOx is one of the most promising inorganic HTLs due to its suitable work function, high optical transmittance, and strong chemical, thermal, and light stability [31]. In this study, NiOx was used.

The NiOx layer was deposited on the substrates using direct current (DC) reactive sputtering of a Ni target in pure oxygen plasma. A basic diagram of sputtering is depicted in Fig 2.3. To optimize its optoelectronic properties, an annealing step at 300°C for 20 minutes in air was performed, improving crystallinity and reducing Ni^{3+} defects.

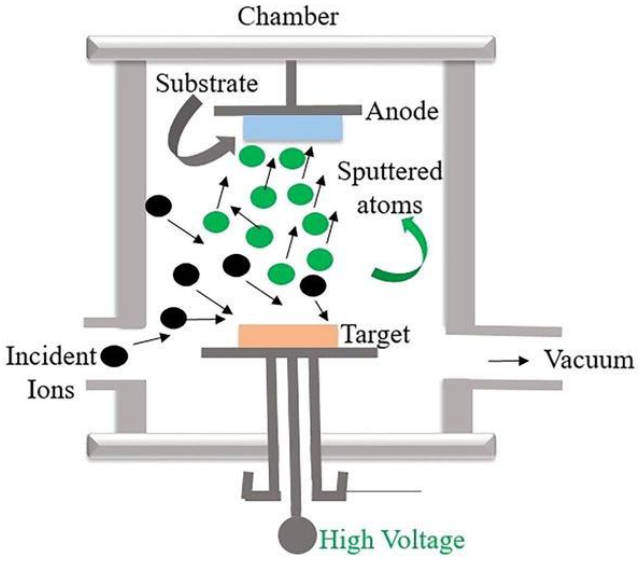

Fig 2.3: Sputtering with Oxygen Plasma [44]

Sputtering (shown in Fig. 2.3) is a physical vapor deposition (PVD) technique where high-energy particles bombard a target material, ejecting atoms that then deposit onto the substrate. This ion bombardment is usually achieved using a pure oxygen plasma[44].

2.3.2 SAMs

As discussed before SAMs are used as both Hole Transport Layer and also as a surface passivation layer to help reduce interface defects. Self-assembled monolayers (SAMs) are single-layer molecular films that spontaneously organize into a structured arrangement without external intervention [45]. This occurs through liquid or vapor-phase deposition onto a substrate. The self-assembly process consists of three stages:

1. Adsorption – Molecules initially adhere to the substrate.
2. Self-Assembly – The molecules organize into an ordered structure.
3. Monolayer Formation – A stable, final monolayer is established.

SAM molecules typically have three key components:

1. Anchoring Group – Ensures strong attachment to the substrate.
2. Spacer Chain – Stabilizes the monolayer, with its length influencing overall properties.
3. Terminal Group – Can be modified to tailor surface characteristics.

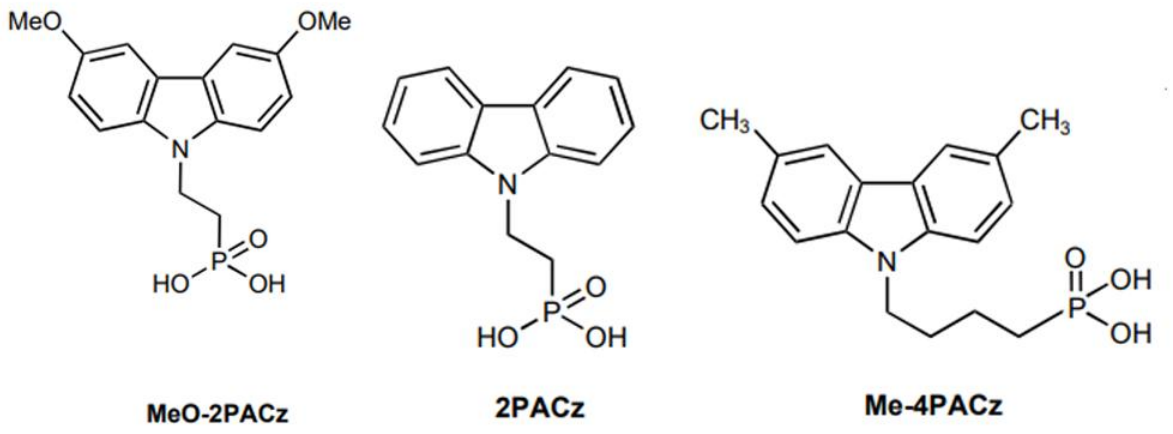

Fig 2.4: SAMs Molecular Structures

SAMs facilitate hole transport while preventing charge accumulation at the interface. They can form ultrathin layers with minimal parasitic absorption and remain chemically stable during perovskite precursor deposition [45]. They do not require extra doping and are compatible with various substrates, making them ideal surface passivation layers between HTL and the perovskite layer as done in this study [45]. Figure 2.4 shows the structures of 3 SAM molecules commonly used in perovskite solar cells. All of these are a part of a family of carbazole based molecules with a phosphonic acid group.

For this project, Me-4PACZ was used in the runs involving spin-coating. There are several methods of depositing SAM molecules including solution processing techniques like spin-coating or blade-coating. But SAM molecules were deposited using thermal evaporation in this study.

Thermal evaporation is a low-pressure process (~5×10^{-5} Pa) where a solid material is heated to produce vapor. This vapor is then deposited onto a substrate, transitioning back into a solid state. A crucible containing the source material is used to facilitate this process [32]. Thus, thermal evaporation eliminates the need for solvents and allows for the fabrication of large-area devices with uniform, pinhole-free surfaces. It also provides precise control over film thickness, which is challenging with spin-coating [32]. Additionally, it helps prevent the formation of trap or defect sites that can arise from solvent-based precursor synthesis [32]. As demonstrated in Fig 2.5, deposition of a single or multiple materials can be done together or sequentially [32].

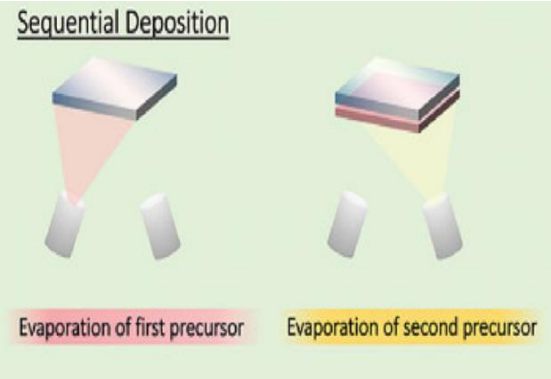

Fig 2.5a) Sequential deposition [32]

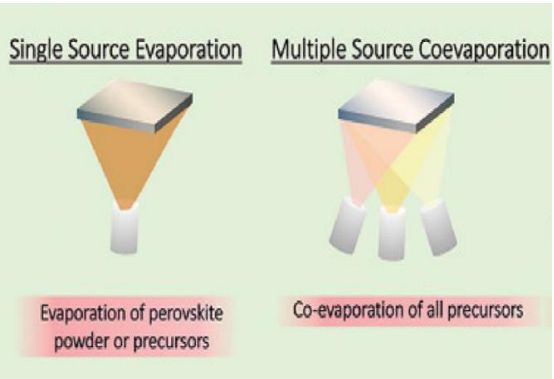

Fig 2.5b) Single and Multiple source Co-evaporation [32]

2.3.3 Perovskite Layer

As mentioned above, hybrid deposition was used in this project where co-evaporation was followed by spin-coating or blade-coating.

2.3.3.1 Co-evaporation

Multiple (Dual) Source Evaporation (depicted in Fig 2.5b) was used with PbI_2 and CsBr as the selected compounds to help build the inorganic scaffold. The substrates are kept at a temperature of -5° C and they are rotated during the simultaneous deposition.

This is followed by the organohalide solution deposition which can be done using either spin-coating or blade-coating. The following section explains the 2 processes.

2.3.3.2 Spin-coating

Spin-coating is a method for depositing thin films with thicknesses ranging from nanometers to micrometers [45]. In this process as shown in Fig 2.6, a liquid solution is dispensed onto a substrate, which is then rapidly rotated. The centrifugal force spreads the solution evenly across the surface, resulting in a uniform coating. The final thickness of the film can be controlled by adjusting the spin speed, duration, and the properties of the solution used [45].

Fig 2.6: Schematic representation of Spin-coating [45]

There are two methods of dispensing the solution:

1. In static spin-coating, the solution is first deposited onto the stationary substrate, and then the spinning process begins
2. In dynamic spin-coating, the solution is dispensed onto the substrate while it is already spinning. In this project, this process was followed.

2.3.3.3 Blade-coating

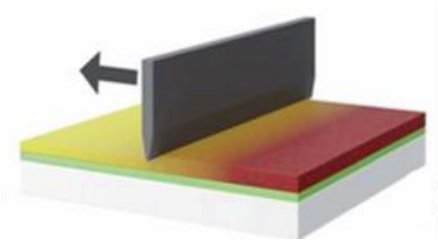

Fig 2.7: Schematic representation of blade-coating

Blade-coating is a method in which a blade moves across a surface and spreads pre dispensed solution across the substrate when moving from one end to another [33]. The initial step in the coating process involves dispensing the precursor solution onto the substrate. During this stage, the wettability of the solution is a key factor, as it significantly influences the spreading behavior

and the subsequent crystallization of the film [34]. Following the wetting process, the solution spreads across the substrate, transitioning from discrete droplets into a continuous film, as depicted in Fig 2.7. The film thickness is influenced by the spreading speed and follows two distinct regimes:

1. Evaporation Regime: When the spreading speed is low, the solvent evaporation rate and the spreading speed occur on a similar timescale. Hence slower speeds lead to thicker films here.

2. Landau-Levich Regime: When the spreading speed is high, the solvent evaporation rate is significantly lower than the spreading speed, leading to a film formation governed by fluid dynamics rather than evaporation. Hence faster speeds lead to thicker films.

The deposition is followed by a thermal annealing step where the substrates are heated to 130° C for 20 minutes to help ensure evaporation of the solvents and improve crystallinity of the perovskite.

2.3.4 Electron Transport Layer

Electron transport layers (ETLs) in p-i-n perovskite solar cells are primarily composed of fullerene-based n-type conjugated polymers or n-type metal oxides. These materials must possess key properties such as appropriate energy levels, high electrical conductivity and mobility, and ease of fabrication[31].

Fullerene-based materials, including C60 and C70, are widely used due to their high electron mobility and low-temperature processability [31]. However, their high cost remains a challenge. Typically, a buffer layer follows the fullerene ETL to optimize energy alignment with the counter electrode [31].

For this work, C60 was chosen as the ETL, with a lithium fluoride (LiF) buffer layer introduced between the perovskite and C60 to improve interfacial quality. Similarly, a BCP buffer layer was used to enhance the contact between C60 and the metal electrode. Both buffer layers along with the C60 layer were deposited via thermal evaporation under high vacuum.

2.3.5 Metal Contacts

To help extract the charge carriers into the external circuit, metal contacts are deposited onto the existing stack. In this project, silver was deposited using thermal evaporation under high vacuum. Before deposition, the ends of the substrates were scratched to provide space for contacts to complete the circuit. Masks are used to deposit the silver precisely.

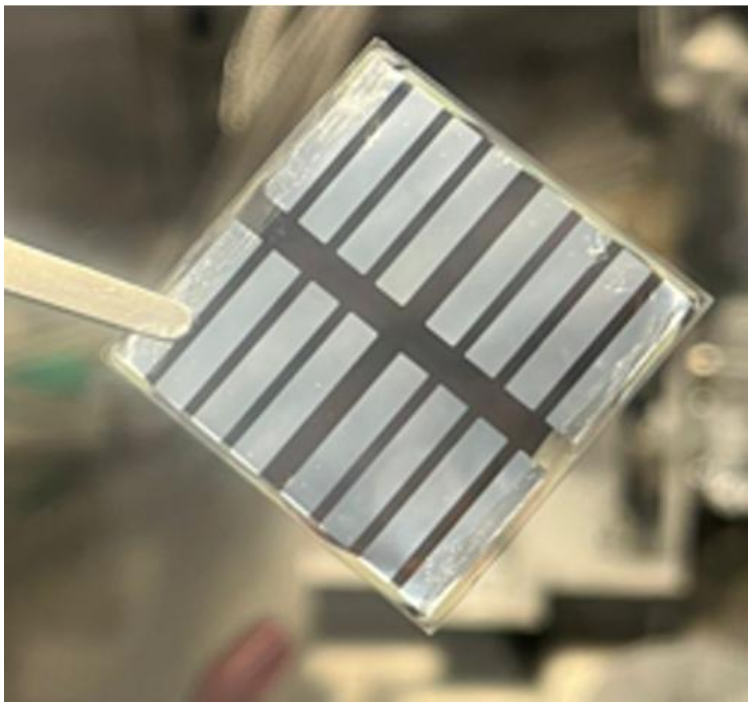

Fig 2.8: A photograph showing the rear electrode side of a single-junction perovskite

2.4 Characterization

Characterizing the solar cell and the perovskite film is an important aspect in understanding how the device performance changes with the different parameter changes. Along with the performance quantifiers described before in Section 1.6, the following characterization techniques help provide an insight into the optoelectronic properties of the devices along with the physical properties of the perovskite film. The techniques used in this project have been described briefly below.

2.4.1 Solar Simulator

A solar simulator is a characterization tool designed to replicate sunlight, enabling the evaluation of solar cell performance. While it has various applications, in this study, it was primarily used to measure the current-voltage (I-V) characteristics of the cells and extract key performance parameters.

To ensure reliable and comparable results, measurements were conducted under Standard Test Conditions (STC), which include:

1. A cell temperature of 25°C.
2. Air Mass (AM) 1.5; AM means the path length to that sunlight travels through the Earth's atmosphere before reaching the surface and AM1.5 is used as a standard because it simulates sunlight when the sun is at a 48.2° angle in the sky, which is representative of average conditions in mid-latitudes. It defines a realistic solar spectrum that includes the effects of atmospheric absorption and scattering.
3. The light intensity is set to one sun illumination (1000 W/m^2), a crucial parameter as solar cell efficiency is influenced by both the incident light spectrum and its intensity.

During operation, a range of voltages is applied to polarize the solar cells, and the resulting current is measured to record the current-voltage (I-V) characteristics[9]. Some measurement systems offer additional features; in this study, an internal fan was used to regulate the device heating under operation.

Solar simulators differ based on the type of lamp used. Here, a xenon lamp was selected for its broad and stable spectrum, which closely replicates natural sunlight.

Hysteresis measurements help detect hysteresis effects in solar cells, where the JV curve varies depending on the voltage sweep direction. This phenomenon is often linked to defects, interface properties, and charge trapping within the device [9].

A maximum power point tracker (MPPT) is used to determine the operating point where the solar cell delivers maximum power [9]. The MPPT algorithm continuously adjusts the voltage to maintain stable power output over time.

2.4.2 Photoluminescence (PL)

Photoluminescence (PL) spectroscopy is a non-contact, non-destructive technique used to examine the electronic properties of materials. By analyzing the intensity and spectral composition of the emitted light, key characteristics such as bandgap energy, impurity levels, and recombination mechanisms can be assessed [36].

The PL spectrum of a semiconductor provides insight into its electronic bandgap, which is crucial for determining its elemental composition and evaluating its suitability for solar cell applications [36]. At low temperatures, PL measurements can reveal peaks associated with impurities and defects, allowing for the detection of both intentional and unintentional contaminants that significantly impact material quality and device performance [36].

Additionally, the intensity of PL emission is directly linked to the competition between radiative and non-radiative recombination processes. Since non-radiative recombination is often caused by defects and impurities, PL spectroscopy serves as a powerful tool for monitoring changes in material quality across different fabrication and processing conditions [36].

In this study, Steady State PL (SSPL) and Time Resolved PL (TRPL) were used to evaluate the bandgap of the different perovskite films, and their respective charge carrier lifetimes.

2.4.3 Scanning Electron Microscopy

The scanning electron microscope (SEM) is a widely used imaging technique that enables the acquisition of high-resolution microstructural images across multiple scientific disciplines[37]. Unlike optical microscopes, which rely on visible light, SEM employs a high-energy electron beam to achieve significantly greater resolution [37]. When the electron beam interacts with the sample, it produces various signals that provide detailed insights into the sample's surface morphology and structural characteristics [37]. A schematic of the same is provided below in Fig 2.9. In this project, perovskite films were investigated using SEM.

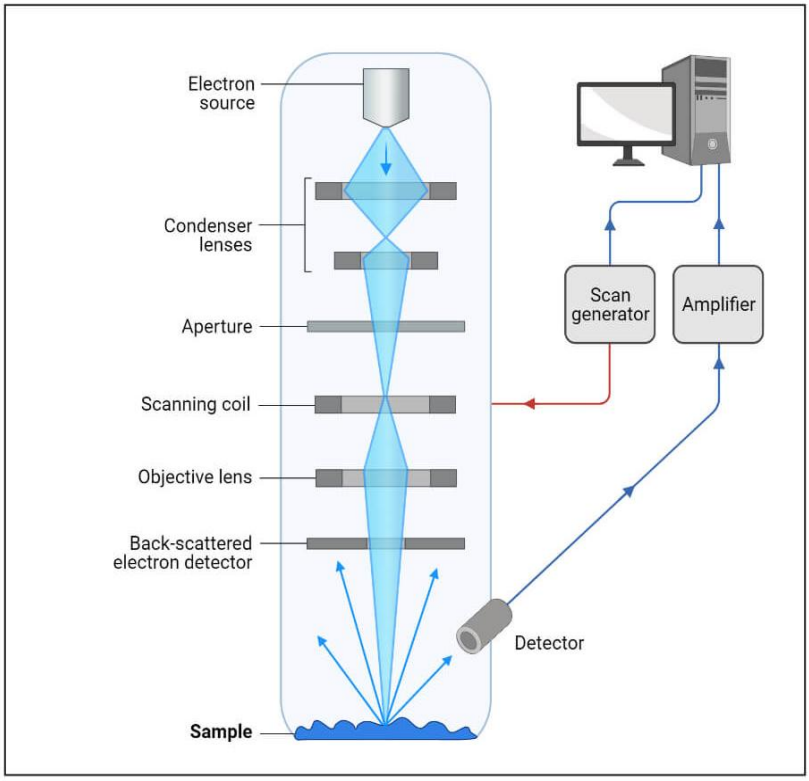

Fig 2.9: Representative Diagram of SEM [38]

Chapter 3: Bulk and Surface Defect Passivation

This chapter begins with an exploration of various additives incorporated during spin-coating, both as bulk additives and surface passivation layers, applied to the pre-existing reference recipe. The resulting performance trends and effects are analyzed through experimental data, with their implications discussed alongside challenges encountered during spin-coating runs.

Following this, the focus shifts to the deposition of organohalide solutions using blade-coating, starting with the optimization of a reference recipe for the same 1.67 eV bandgap samples. The discussion then expands to the role of MACl in perovskite film growth, understanding its influence on crystallization and film morphology using different characterization tools. Subsequently, the selection of solvents for blade-coating is examined using various characterization techniques to assess their impact on film formation.

Finally, the chapter explores surface passivation using blade-coating, detailing the optimization process, resulting device performance, and efforts to understand film passivation through various characterization techniques.

3.1 Spin-coating

Having covered the spin-coating process in the previous chapter, this section shifts focus to the reference recipe and the additives explored to enhance perovskite solar cell performance, along with their corresponding results.

3.1.1 Reference Recipe:

In this study, mostly the co-evaporation ratio of 1:0.1 PbI2:CsBr was used for the inorganic scaffold as it leads to better conformality on textured silicon. This ratio, found in an earlier study, was kept constant through most of the sample batches.

For all the spin-coating runs, 230 nm of PbI2 while proportionately 23 nm of CsBr were deposited in the co-evaporation chamber.

The organohalide solution was made of 50% FABr (0.196M) to 50% FAI (0.196 M) and 0.101 M MACl (25.8% of total solution of FAI+FABr). After stirring for 30 minutes, the solution was spin-

coated onto the samples at 2100 rpm. After the process, the samples are kept for drying for 10 minutes followed by 20 minutes of annealing in air (outside the glovebox) at 130°C.

3.1.2 Bulk Modification

Bulk additives are added to the organohalide solution itself and therefore spin-coated with the organohalide solution. While MACl can be identified as a bulk additive, a detailed study on the same was done during the blade-coating depositions. The other additive tried is shown below with the results obtained.

3.1.2.1 pFBPA

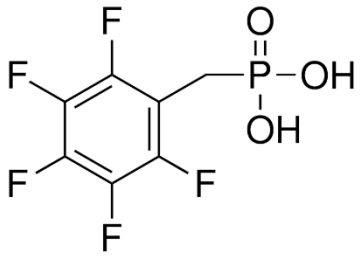

Fig 3.1: Molecular Structure of pFBPA

The first bulk additive chosen for this study was 2,3,4,5,6-pentafluorobenzylphosphonic acid (pFBPA) with its molecular structure shown in Fig 3.1. According to Chin et al. [39], X-ray photoelectron spectroscopy (XPS) analysis indicated that this additive interacts with Pb^{2+}/Pb^{0} surface defects. The phosphonic group in FBPAc binds to these lead-related defects, thereby minimizing non-radiative recombination states at the material's top surface [39]. Furthermore, their findings suggest that incorporating this bulk additive reduces interfacial strain at the perovskite/ETL interface, which can arise due to lattice mismatch, thermal expansion differences, or film stress during crystallization. By relieving this strain, the additive improves film stability and charge transport, while also promoting the formation of larger perovskite domains, which can further enhance carrier lifetimes and overall device performance.

In the referenced study, [39] they used a pFBPA stock solution concentration of 5 mM (around 1.3 mg/mL) dissolved in ethanol and then added directly to the powders. A very similar approach was used in this work: a stock solution of 2 mg/mL dissolved in ethanol was either added directly to the powders or further diluted with ethanol to achieve the desired concentration of pFBPA. The evaporation rates in this run were 2:0.6 A/s PbI_2: CsBr (230 nm:69 nm). SAMs were also used as an interlayer between the HTL and the perovskite layer for the runs involving pFBPA as a bulk additive.

The concentrations of pFBPA used were 50 ug/ml and 100 ug/ml. The following Figure 3.2 shows how the cells fared against reference cells (ref) (i.e. without any pFBPA). As demonstrated, the V_{oc} improved slightly when 100 ug/ml was used, while the other parameters were comparable to the references in most of the cells leading to a small improvement in efficiency. Due to not well-defined cell active area by the metal electrodes in 2 of the samples, their current density was high.

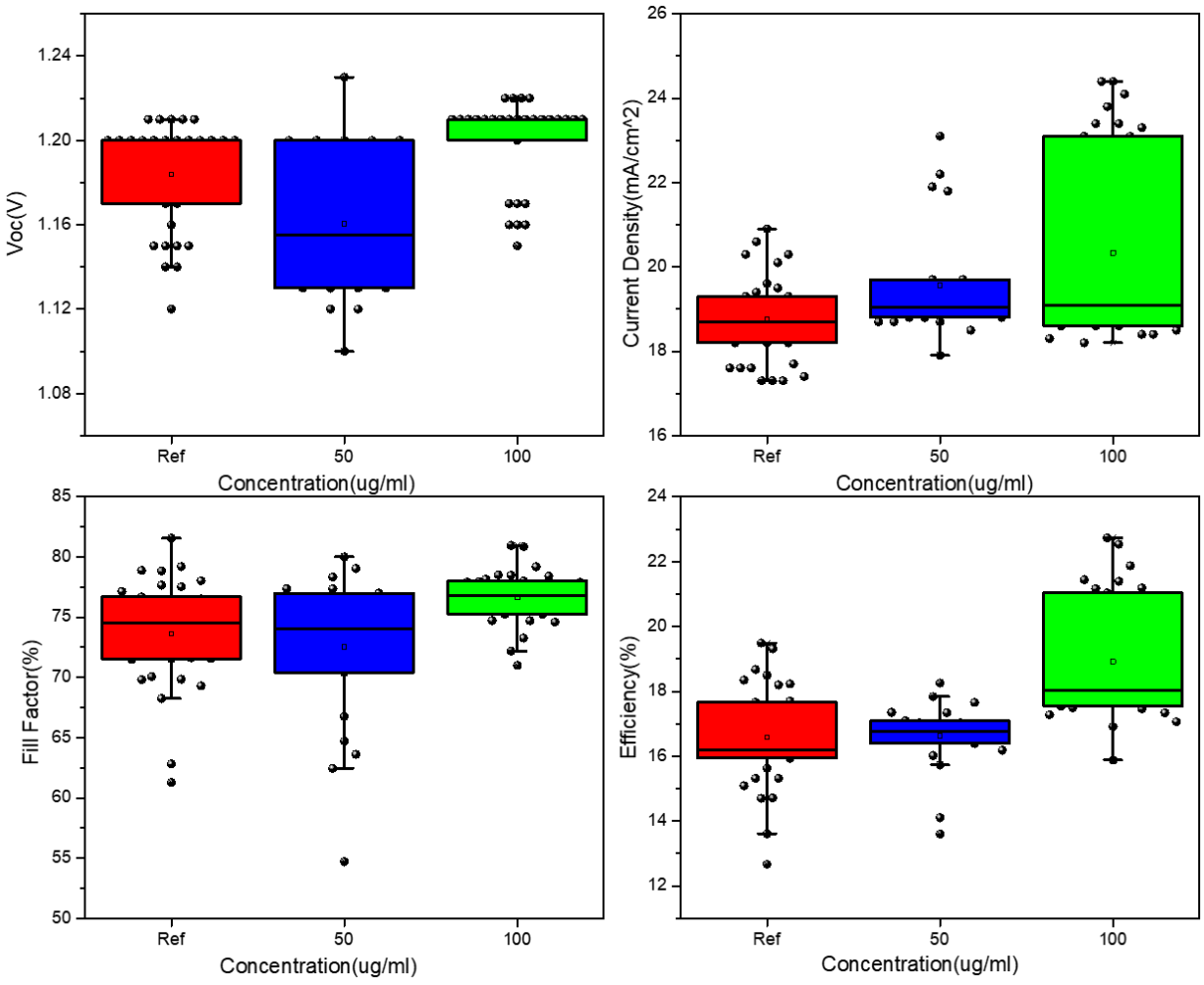

Fig 3.2: Photovoltaics parameters of the cells without(Ref) and with pFBPA as bulk additive at concentrations of 50 and 100 ug/ml

To evaluate the stability of the fabricated perovskite solar cells under continuous illumination, each cell was subjected to continuous AM 1.5G illumination and measured every 2 minutes during a 10-minutes exposure, each cell was subjected to continuous light exposure and measured every 2 minutes during a 10-minutes exposure.

Figure 3.3 illustrates the evolution of device performance parameters under prolonged illumination. A noticeable increase in V_{oc} is observed with light soaking, with a more pronounced enhancement in the 100 µg/mL pFBPA treated sample compared to the 50 µg/mL counterpart. However, while the Jsc of the reference sample remains relatively stable, a decline is observed in the 50 µg/mL pFBPA treated sample, with a larger reduction in the 100 µg/mL pFBPA sample. Similarly, the FF remains largely unchanged for both the reference and the 50 µg/mL sample, whereas a reduction is noted for the 100 µg/mL sample. Consequently, while the reference device exhibits an improvement in PCE upon light soaking, both pFBPA-treated samples show a decline in overall device efficiency.

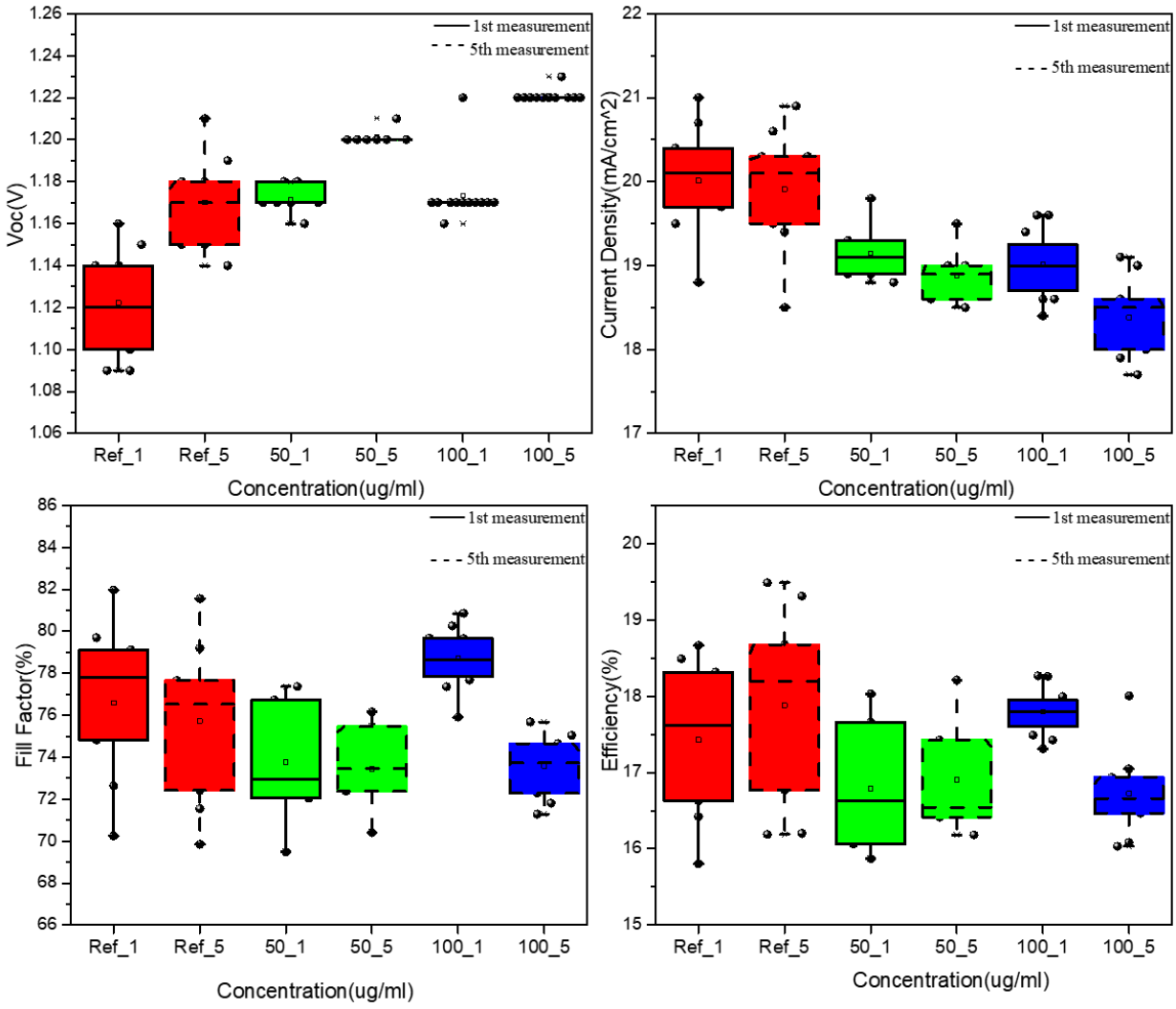

Fig 3.3: First (denoted as _1) and Fifth (denoted by _5) measurements of cells (under prolonged illumination to observe light soaking effects) without(Ref) and with pFBPA as bulk additive at concentrations of 50 and 100 ug/ml

Around the same time, a parallel study in our lab determined that a PbI_2:CsBr ratio of 1:0.1 A/s(230:23 nm) in the hybrid deposition process improved PbI_2 porosity and resulted in higher conformality on textured silicon surfaces. Consequently, all subsequent depositions were performed using this optimized ratio.

Building on this, the previously tested pFBPA concentrations were tried out using the 1:0.1 PbI_2:CsBr evaporation ratio. Figure 3.4 presents the performance of the solar cells fabricated using the optimized PbI_2:CsBr evaporation ratio. While an increase in current density and FF is observed, the primary objective of passivation was to enhance the V_{oc}. However, as shown in Figure 3.4, the V_{oc} for the 50 µg/mL pFBPA sample is lower than that of the reference, while the improvement for the 100 µg/mL sample remains minimal. Altogether, the PCE has improved for the pFBPA samples.

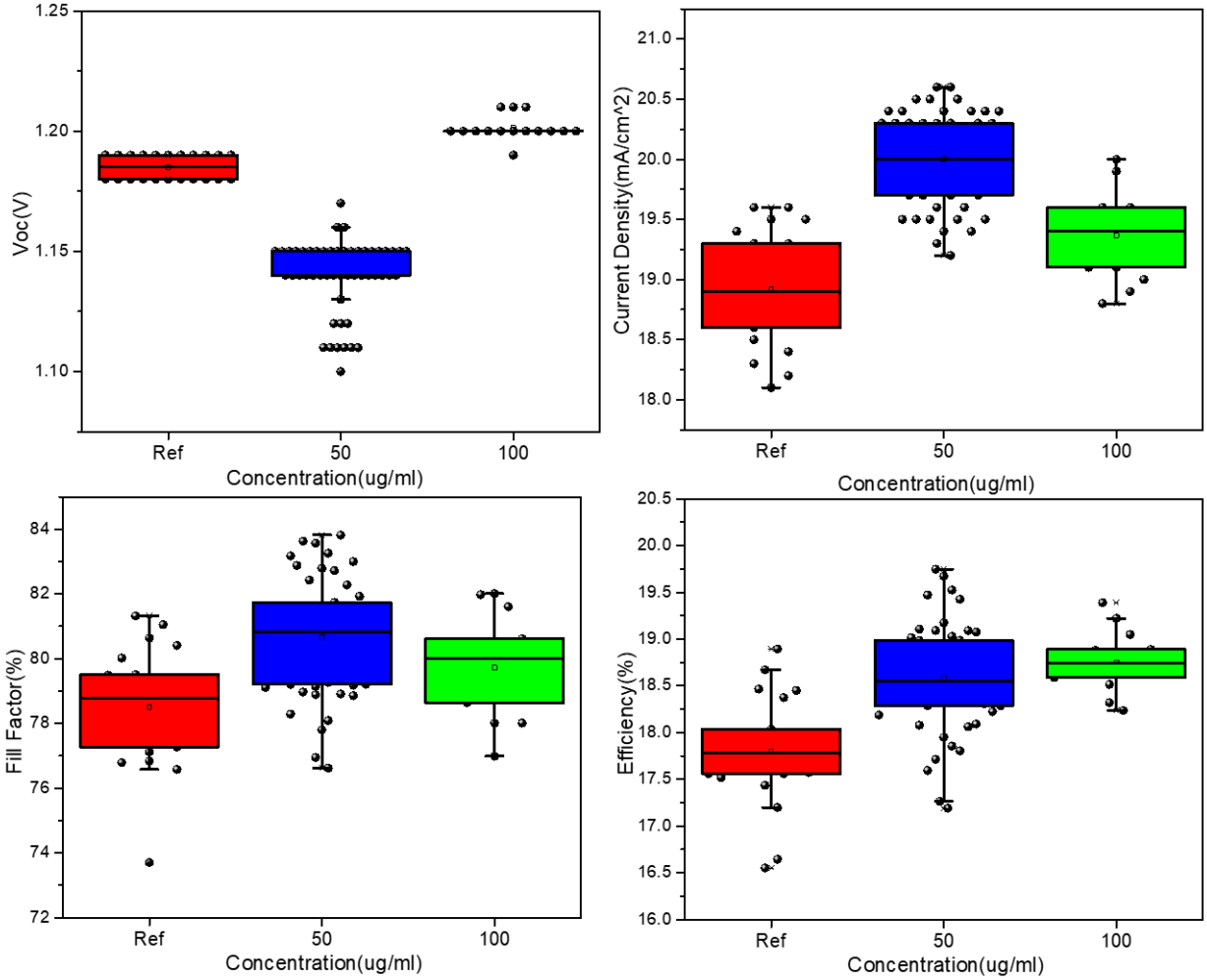

Fig 3.4: Photovoltaics parameters of the cells without(Ref) and with pFBPA as bulk additive at concentrations of 50 and 100 ug/ml

3.1.3 Surface Modification

The objective of these experiments was to enhance device performance by modifying the perovskite surface through a targeted surface treatment. This was achieved by spin-coating a passivator-containing solution onto the perovskite layer. The fabrication process remained consistent with the standard procedure up to the perovskite annealing step. Following annealing, the surface passivation layer was deposited via spin-coating, followed by a brief post-treatment annealing step at 100°C for 5 minutes. While perovskite annealing was conducted in air (on the wet bench to maintain controlled temperature and humidity conditions), the post-passivation annealing was performed inside the glovebox to minimize exposure to ambient conditions. The ETL deposition and subsequent fabrication steps followed the previously established protocol.

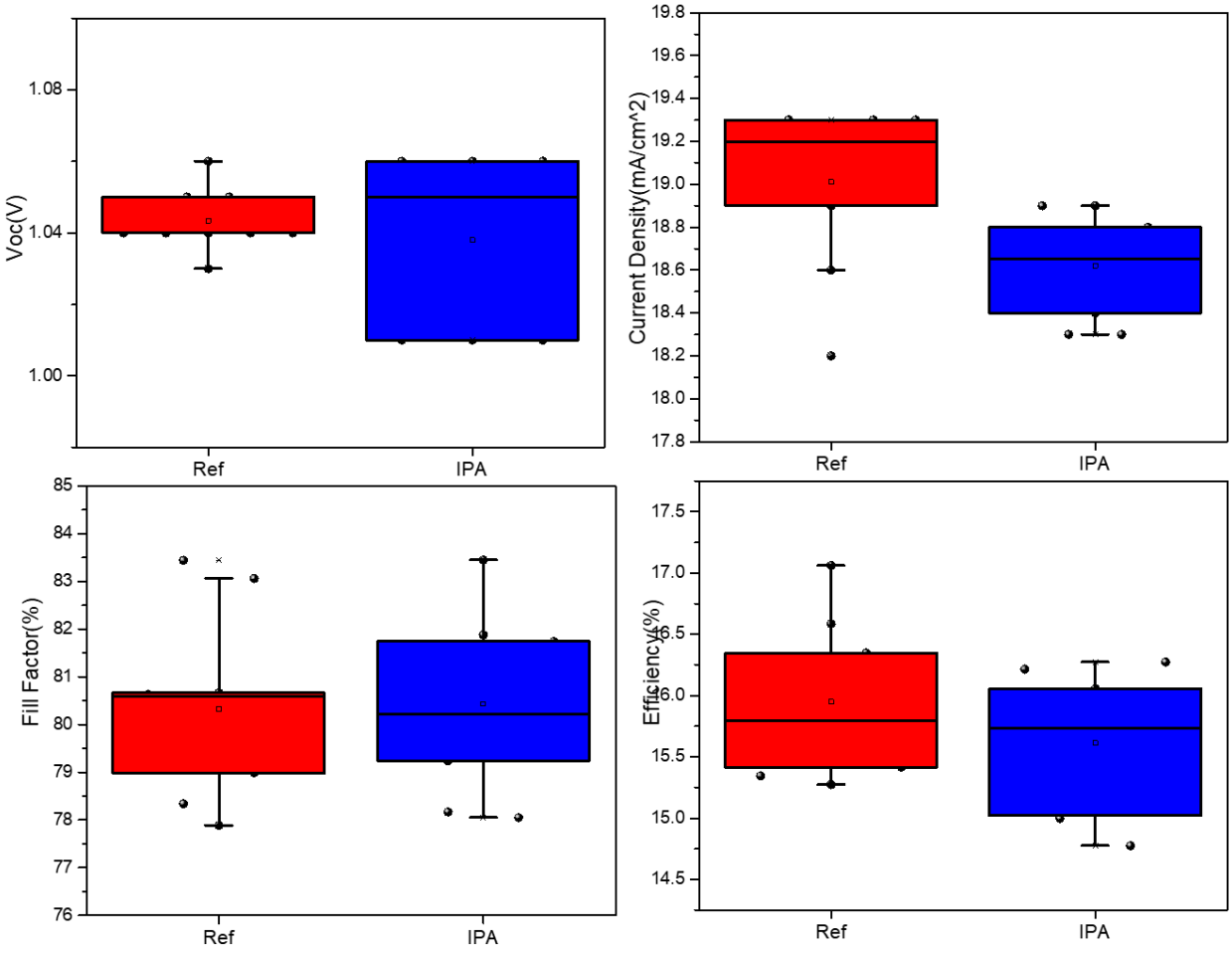

Fig 3.5: Photovoltaics parameters of IPA coated cells vs Reference Cells

Previous studies have shown that ethanol-based solutions can negatively impact perovskite crystallinity and overall device performance. As a result, isopropanol (IPA) was explored as an alternative solvent for the surface passivation layers. To confirm that IPA itself did not introduce any adverse effects, a control experiment was conducted where a layer of pure IPA was spin-coated onto the perovskite film, following the same procedure used for passivation molecules. Figure 3.5 presents the performance comparison between the IPA-coated sample and an uncoated perovskite cell, showing that the two exhibit nearly identical characteristics. This indicates that IPA does not cause notable degradation of the perovskite film and is suitable for use in the passivation process.

In addition to exploring pFBPA as a surface passivation layer, a literature review identified other potential passivation materials, including Piperazinium Iodide (PI) [43] and diammonium ligands such as Propane-1,3-diammonium iodide ($PDAI_2$) [42] and Ethane-1,2-diammonium iodide ($EDAI_2$) [42]. These additives were systematically tested on our samples, and their results are presented in the following sections.

3.1.3.1 pFBPA

Turkay et al. [40] investigated the use of pFBPA as a bulk additive and reported promising results. Their secondary ion mass spectroscopy (SIMS) analysis revealed that pFBPA predominantly accumulated at the top and bottom interfaces of the perovskite film, with relatively low incorporation within the bulk. Given that interface defect densities are typically an order of magnitude higher than bulk defects, this observation aligns with the expectation that pFBPA could effectively mitigate interfacial recombination. These findings motivated us to explore pFBPA as a dedicated surface passivation layer rather than a bulk additive.

A 0.1 mg/ml pFBPA solution was prepared by diluting the stock solution of 0.5 mg/ml. Selecting an appropriate spin-coating speed is crucial for achieving effective surface passivation, as it influences the thickness, uniformity, and coverage of the passivation layer. Higher spin speeds result in thinner films, potentially improving uniformity but reducing passivation efficacy, whereas lower speeds may lead to thicker deposition, altering charge transport and interfacial defect passivation. To evaluate these effects, three different spin-coating speeds—2500 rpm, 3500 rpm, and 4500 rpm—were investigated.

Figure 3.6 presents the results for different spin-coating speeds compared to reference cells without passivation treatment.

Across different spin-coating speeds, the V_{oc} remained relatively unchanged. The current density for the 2500 rpm and 3500 rpm samples was comparable to that of the reference cells, while the Jsc did not decline for any of the samples. The FF of the 4500 rpm and 3500 rpm samples matched

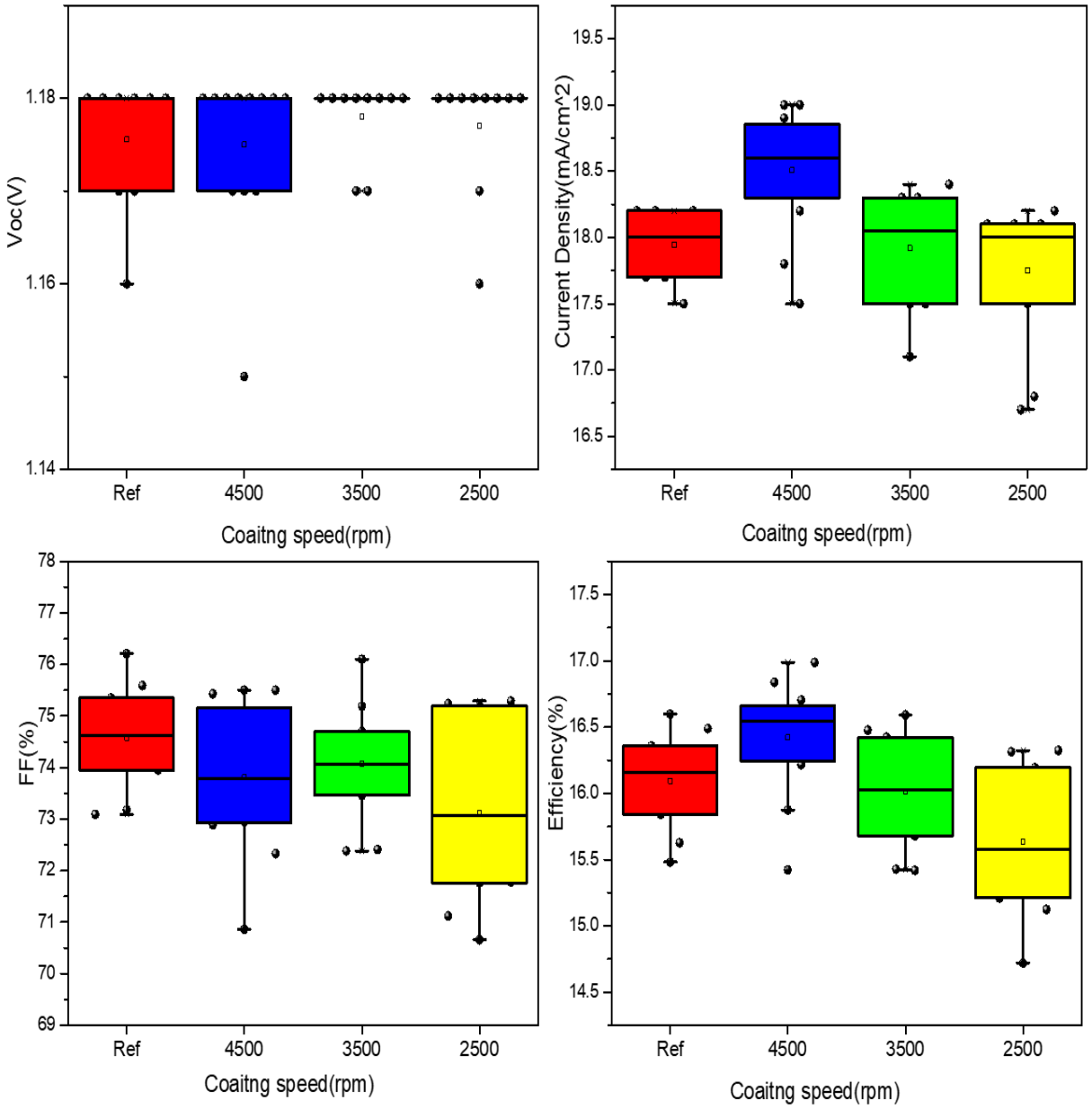

Fig 3.6: Photovoltaics parameters of the cells without (Ref) and with pFBPA as surface passivation layer at different spin-coating speeds (in rpm)

the reference, whereas the 2500 rpm sample showed a slight decline. Although, the 4500 rpm condition yielded the highest efficiency, the results were not entirely conclusive as the differences were quite small between different speeds. Thus, 4500 rpm was selected as the coating speed and the concentration varied in subsequent batches.

Concentrations of 0.1, 0.3, and 0.7 mg/ml of pFBPA were tested at 4500 rpm, as shown above in Fig. 3.7. While V_{oc} exhibited an increasing trend with higher concentrations, the current density was lower for all treated samples compared to the reference. The FF showed a slight improvement

across all concentrations. Consequently, the overall efficiency of the pFBPA-treated samples remained comparable to the reference cells, with the highest-performing samples observed at 0.7 mg/ml. However, as can be seen, the efficiency across this batch was lower than the other batches (e.g. the batch in Fig. 3.6).

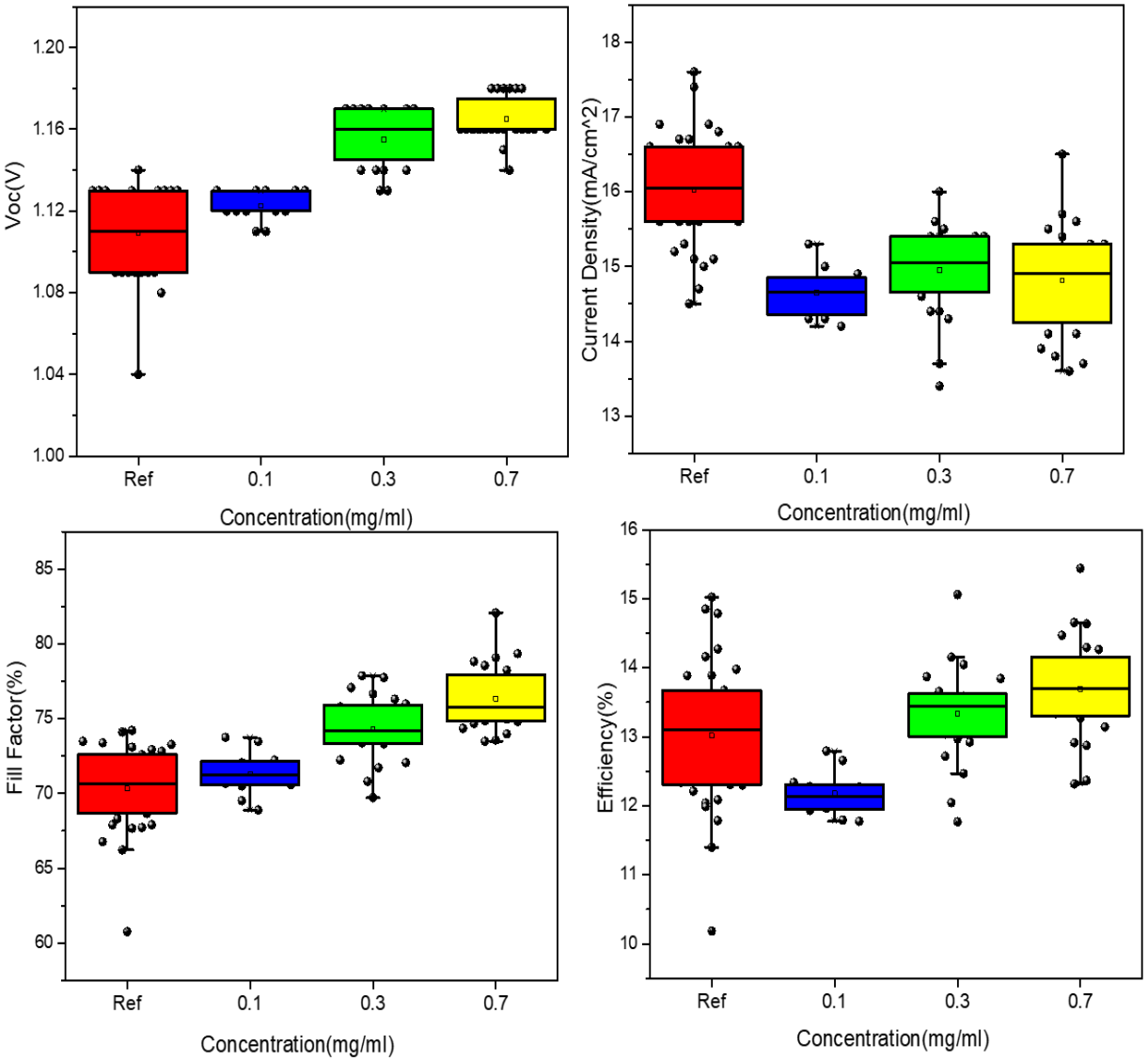

Fig 3.7: Photovoltaics parameters of the cells without (Ref) and with pFBPA as surface passivation layer at different concentrations of 0.1, 0.3 and 0.7 mg/ml

3.1.3.2 PI

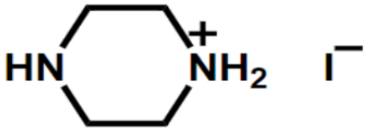

Fig 3.8: Molecular Structure of PI

As found by Li et al. [43], Piperazinium iodide (PI) is an effective surface passivation agent for inverted perovskite solar cells (PSCs) due to its dual functionality in defect passivation and energy level modulation [43]. Structurally, PI contains both neutral R_2NH and cationic $R_2NH_2^+$ groups, enabling it to interact with undercoordinated Pb^{2+} sites on the perovskite surface via Pb–N bond formation [43]. This interaction effectively passivates defects, thereby reducing nonradiative recombination losses. Additionally, PI was found to introduce a positive interfacial dipole, which increases the perovskite work function and optimizes band alignment at the perovskite/ETL interface [43]. These combined effects facilitate efficient electron extraction, enhance V_{oc} and contribute to higher PCE.

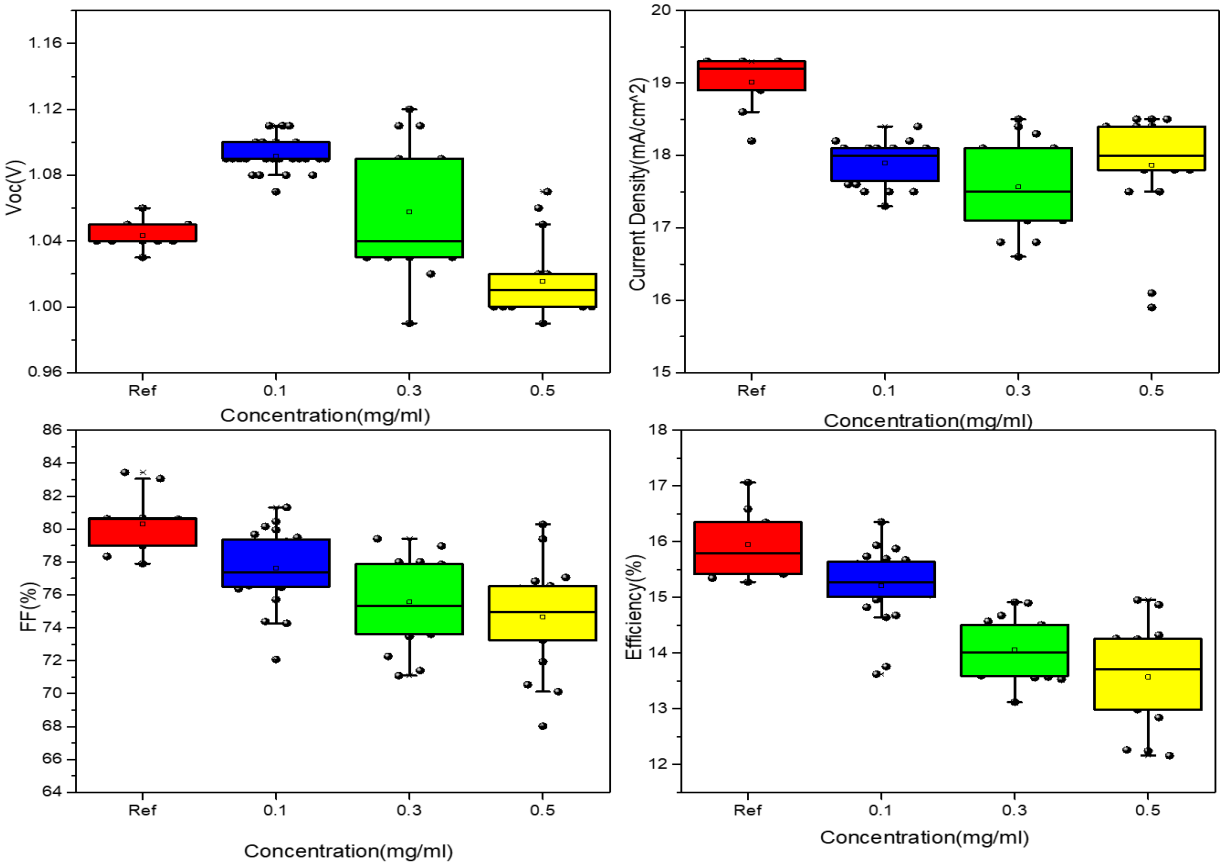

Fig 3.9: Photovoltaics parameters of the cells without (Ref) and with PI as surface passivation layer at concentrations of 0.1, 0.3, 0.5 mg/ml

Thus, we used PI as a surface passivation layer. As done before, solutions of 0.1, 0.3 and 0.5 mg/ml were made from a stock solution of 1.2 mg/ml for concentration screening with the results shown in Fig 3.9. A notable enhancement in V_{oc} was observed for the 0.1 mg/mL and 0.3 mg/mL samples, whereas the 0.5 mg/mL sample exhibited a V_{oc} similar to the reference device. However, the current density was lower across all PI-treated samples compared to the reference, possibly due to excessive surface coverage introducing a resistive barrier to charge extraction. Additionally, the FF exhibited a decreasing trend with increasing PI concentration, suggesting a rise in series resistance perhaps due to excessive surface coverage. As a result, while PI passivation provided some initial improvements, the efficiency remained lower than the reference, with increasing PI concentration further reducing the PCE.

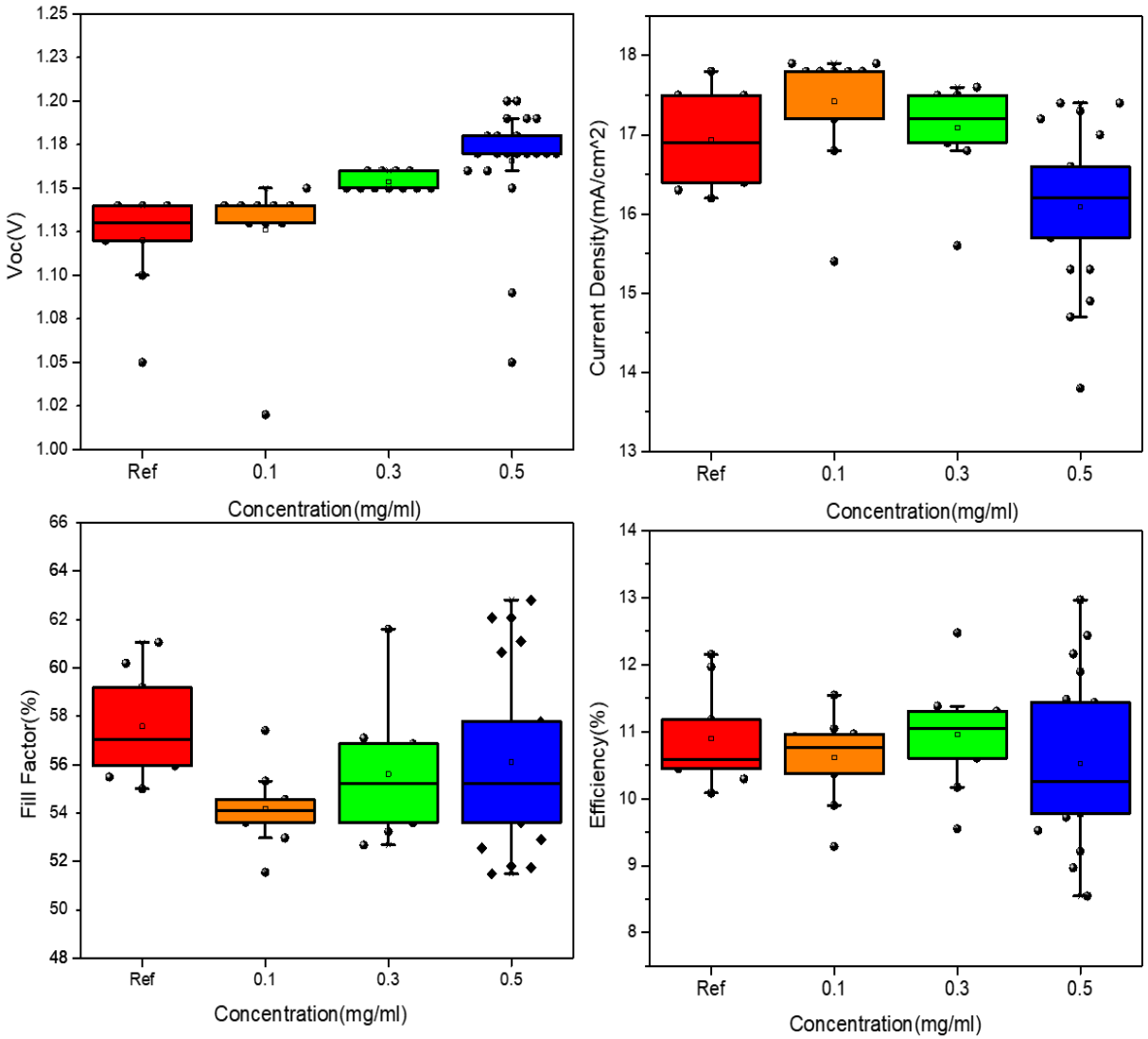

Fig 3.10: Photovoltaics parameters of the cells without (Ref) and with PI as surface passivation layer at concentrations of 0.1, 0.3, 0.5 mg/ml followed by rinsing

As pointed out by Marriotti et al. [41], after the surface passivation layer is annealed rinsing with IPA and then annealing for 5 minutes helps improve device performance. The reasoning behind this step is to remove excess, unbounded PI molecules which may have formed agglomerates and are blocking the charge transport layers [41]. Apart from washing away the excess molecules, it also helps unreacted PI molecules to reach the right positions to bind in the film and help reduce non-radiative recombination [41]. Thus, the same rinsing procedure was followed with the PI concentrations screened previously to see the effect of rinsing. Fig 3.10 shows the performance of different samples against the reference.

A gradual increase in V_{oc} was observed with higher PI concentrations. However, this was accompanied by a decline in current density, which may indicate increased resistance to charge extraction at higher concentrations. Meanwhile, the FF remained relatively consistent across different concentrations but was noticeably lower than that of the reference device. As a result, the PCE of the passivated samples remain fairly similar to the reference cells. Although the trends were noticeable, the batch had an overall lower efficiency.

3.1.3.3 PDAI2

Fig 3.11: Molecular structure of $PDAI_2$

As reported by Liu et al. [42] Propane-1,3-diammonium iodide ($PDAI_2$) can be used as a surface passivation agent to mitigate interface recombination at the ETL interface. As a diammonium compound, $PDAI_2$ introduces a strong surface dipole, which repels holes from the interface while enhancing electron extraction [42]. This effect reduces nonradiative recombination losses, leading to an improvement in V_{oc} and overall device efficiency. Additionally, $PDAI_2$ modifies the energy landscape at the interface, reducing downward band bending at the perovskite/ETL junction and thereby lowering the energy barrier for electron transfer [42]. Prior studies have demonstrated that $PDAI_2$ induces an n-type shift in the surface electronic properties of the perovskite, contributing to better charge transport and interface stability [42].

A stock solution of 1.5 mg/mL was diluted to prepare working solutions of 0.1, 0.2, and 0.4 mg/mL for concentration-dependent screening of passivation effects. The photovoltaic performance of the corresponding devices is presented in Figure 3.12. The variation in concentration did not yield a significant enhancement in V_{oc} across the tested samples. However, a systematic decrease in short-

circuit current density was observed with increasing concentration, implying that excessive passivation may have hindered charge transport at the interface. Furthermore, the FF of the 0.1 mg/mL sample exhibited a marginal improvement compared to the reference devices, whereas higher concentrations (0.2 and 0.4 mg/mL) resulted in a decline in FF, potentially due to increased interfacial resistance or charge extraction barriers introduced by higher concentration of the additive. Consequently, the PCE decreased with increasing passivation concentration.

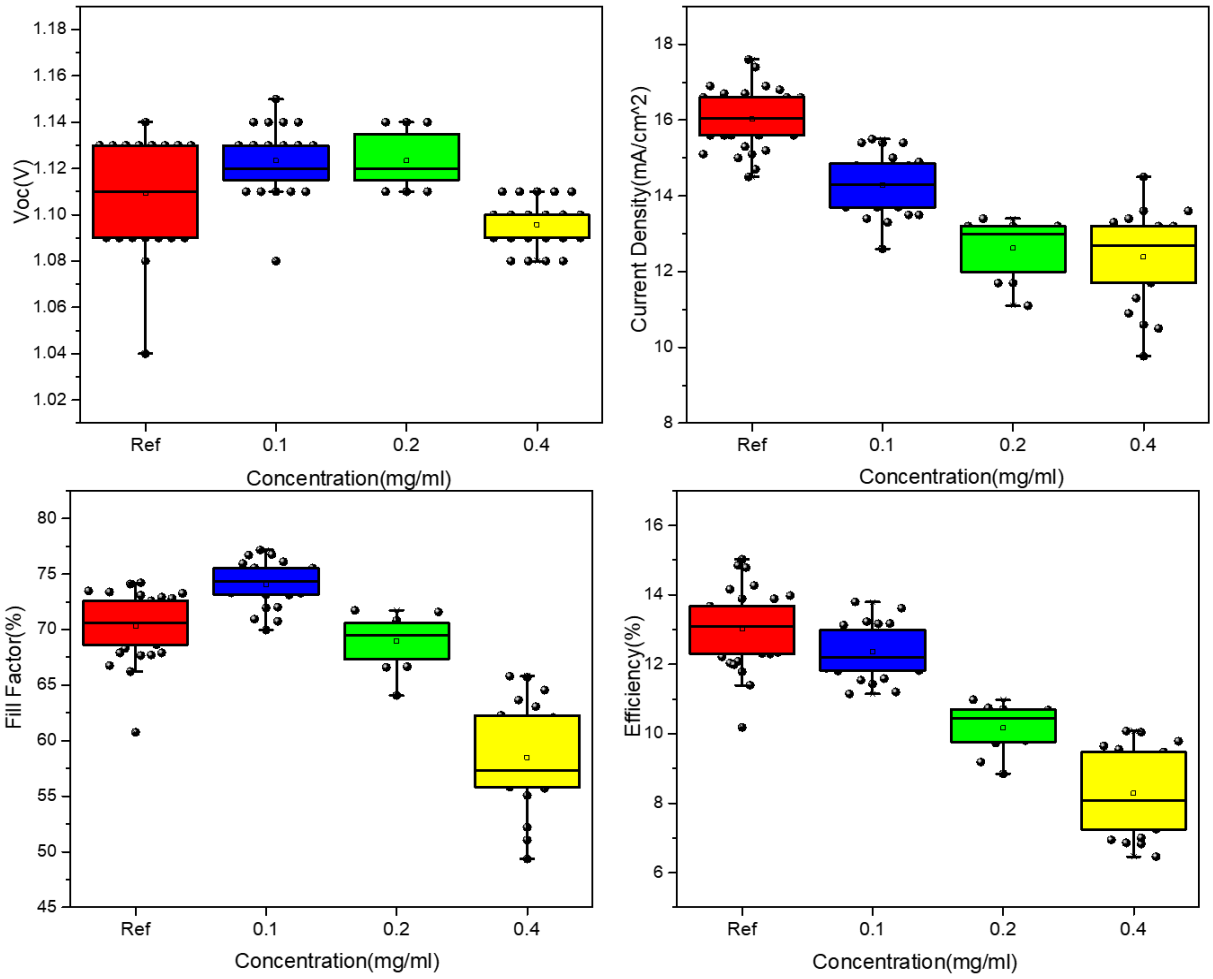

Fig 3.12: Photovoltaics parameters of the cells without (Ref) and with $PDAI_2$ as surface passivation layer at concentrations of 0.1, 0.2, 0.4 mg/ml

3.1.4 Problems with Spin-coating

The initial plan was to first develop an optimized single-junction wide-bandgap perovskite solar cell with a well-passivated layer to enhance V_{oc}, followed by fabricating and optimizing perovskite on textured silicon bottom cells. Blade-coating, a scalable deposition method, was originally

intended to be introduced later in the process as a step toward transitioning from lab-scale spin-coating to a more industrially viable approach.

In the initial phase of this work, spin-coating was used to screen passivating materials and establish general optimization trends. Spin-coating, when performed under well-controlled conditions, is known for its reproducibility. However, during the course of this work, batch-to-batch variations were observed in passivated samples and, at times, even in reference devices. These variations were likely influenced by processing factors such as solution dispensing, wetting behavior, and environmental conditions, rather than fundamental limitations of spin-coating itself. While these factors can be managed with greater process control, they introduced some variability in the results obtained.

Given the long-term goal of developing a scalable fabrication process, blade-coating was introduced earlier than initially planned. While spin-coating remains a valuable technique for small-area optimization, blade-coating offers greater control over film uniformity and drying dynamics in large-area processing. This transition helped mitigate some of the processing inconsistencies encountered and aligned better with the objective of achieving a more scalable and industry-relevant deposition process.

3.2 Optimizing Blade-coating Baseline

Without an optimized recipe for blade-coating, the organohalide concentration was adjusted based on previously optimized one-step deposition protocols established in the lab. A total organohalide concentration of 0.62 M was used, consisting of 0.31 M FAI and 0.31 M FABr, along with 0.16 M MACl (maintaining the 25.8% MACl ratio used in spin-coating). One of the primary parameters in blade-coating is coating speed. Hence to select the optimum speed, samples were blade-coated at 10 mm/s, 15 mm/s, and 20 mm/s, and their results were compared against a spin-coated reference (as can be seen in Fig 3.13).

The V_{oc} of the 10 mm/s (Red) sample is the highest among the blade-coated samples and remains comparable to that of the spin-coated reference. However, V_{oc} decreases with increasing coating speed. In terms of current density, the 10 mm/s and 15 mm/s samples exhibit higher values than the spin-coated sample, suggesting improved charge collection at these speeds. Despite this, the FF of all blade-coated samples is lower than that of the spin-coated reference, with a progressive decline in FF as coating speed increases. Consequently, while the PCE of the blade-coated devices remains lower than the spin-coated sample, a clear trend emerges, with the 10 mm/s sample demonstrating the highest PCE among the blade-coated variants.

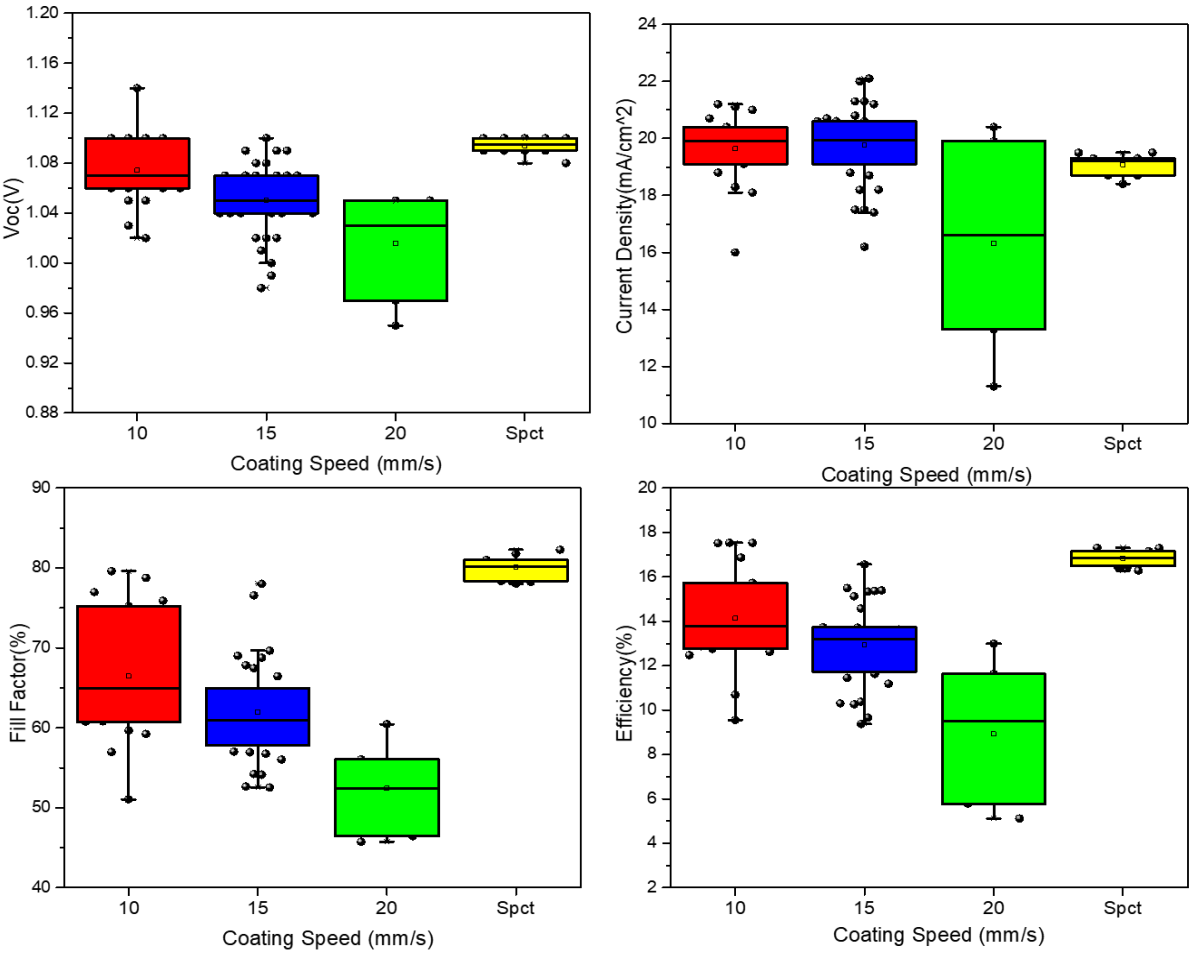

Fig 3.13: Performance of samples coated with different speeds (in mm/s) by blade-coating against a spin-coated reference (spct)

The better operating devices by blade-coating and the spin-coated reference were put for bandgap testing using SSPL and the plots are displayed below in Fig 3.14. While the spin-coated sample revealed a desired 1.67 eV bandgap as seen in Fig 3.13, the 10 mm/s blade-coated sample had a 1.65 eV bandgap and the 15 mm/s coated sample had an even lower bandgap of 1.64 eV. Hence to get the appropriate bandgap of 1.67 eV for monolithic perovskite/silicon tandem cell application, the bromine concentration in the perovskite crystal needed to be increased.

Having an optimized coating speed, the focus was shifted towards the organohalide solution concentration. Seeing lower performance compared to the spin-coated sample along with discoloration from the usual perovskite color indicated excess organics in the perovskite. Fig 3.15 shows the presence of such excess organics in certain spots in the film and was reason enough to lower concentration. Also, the ratio of FABr: FAI was increased to 55:45 to address the bandgap problems that were mentioned above.

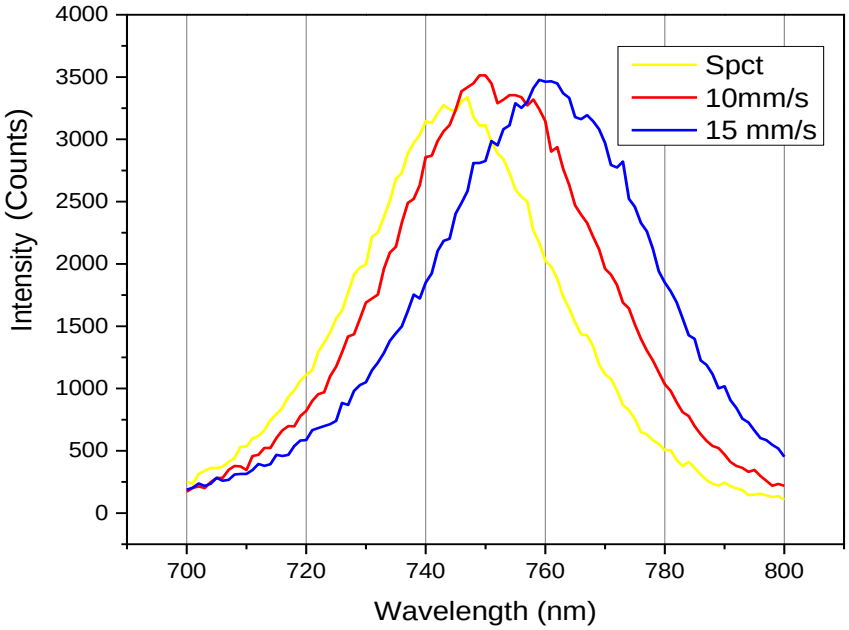

Fig 3.14: SSPL measurements of samples coated with different speeds of blade-coating against the spin-coated sample (spct)

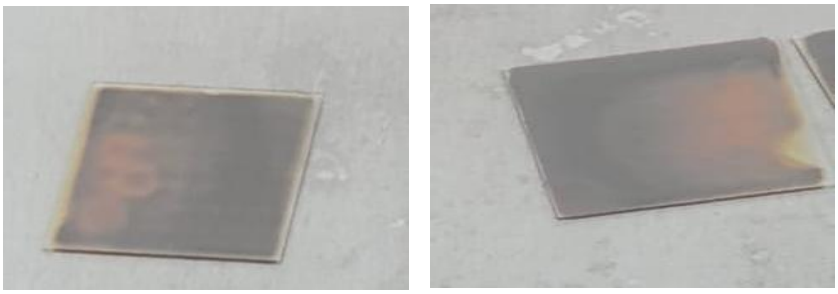

Fig 3.15: Visible discoloration from the ideal dark brown perovskite film color

With the new organohalide concentration ratio (Note: The MACl content was kept the same at 25.8%) a 0.53 M solution was prepared and subsequently diluted with IPA to obtain 0.37 M, 0.41 M, 0.45 M, and 0.49 M solutions. The performance of samples with varying concentrations is presented in Figure 3.16.

The V_{oc} is highest for the 0.41 M sample, while the other concentrations exhibit slightly lower values. Similarly, the current density reaches its maximum at 0.41 M, whereas the FF increases from 0.37 M to 0.41 M before slightly decreasing at higher concentrations. As a result, the PCE peaks at 0.41 M and declines with further increases in concentration.

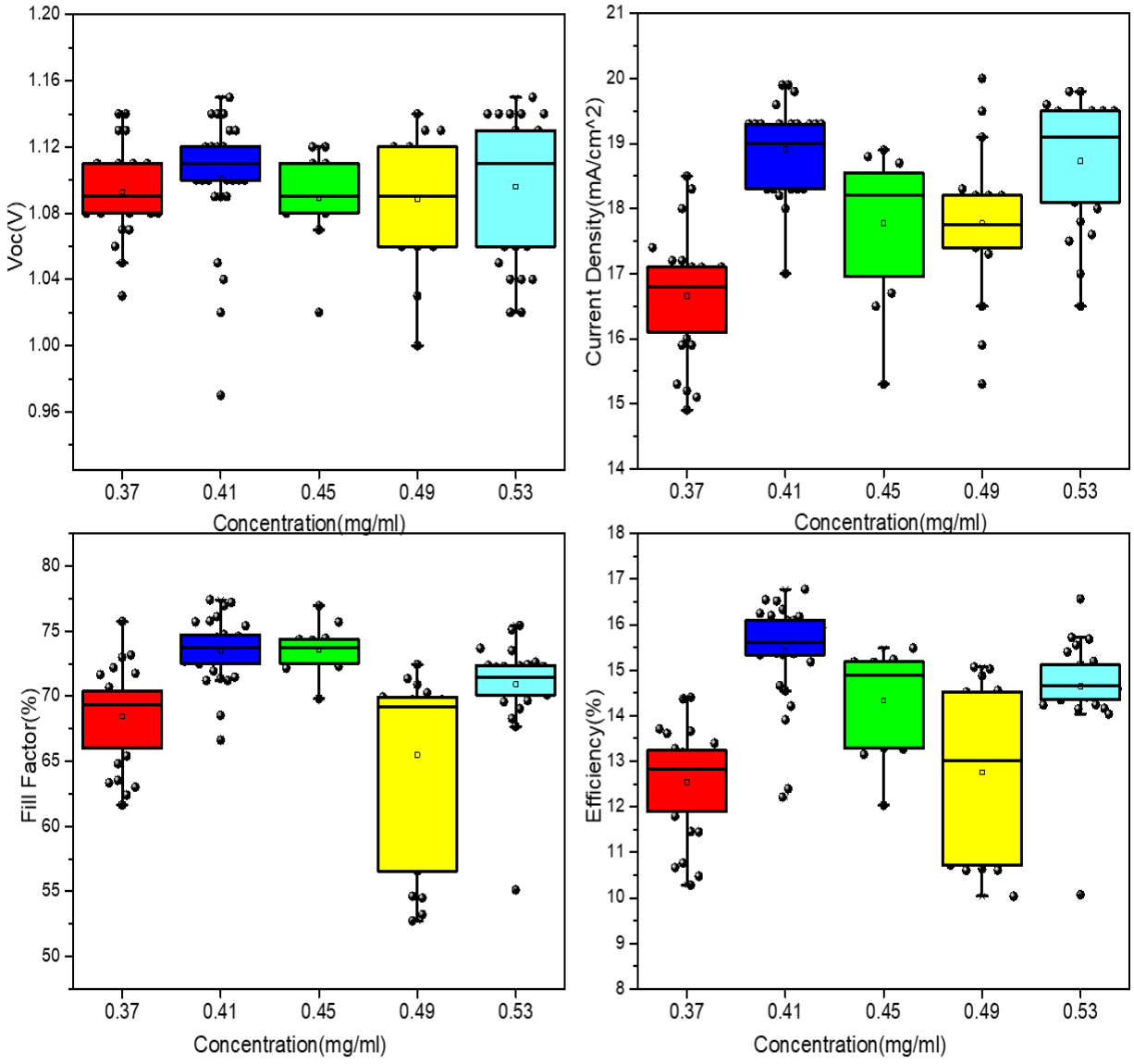

Fig 3.16: Photovoltaics parameters of the cells with organohalide concentrations at 0.37, 0.41, 0.45, 0.49 and 0.53 M

Also, PL measurements were done for some of the samples to check if the 1.67 eV was attained. Fig 3.17 highlights the bandgap for all the samples to be in the 1.67 eV range. Also, the intensity of the PL signal is highest for 0.41M compared to 0.37 M and 0.46 M implying a higher perovskite crystal quality in the 0.41 M sample.

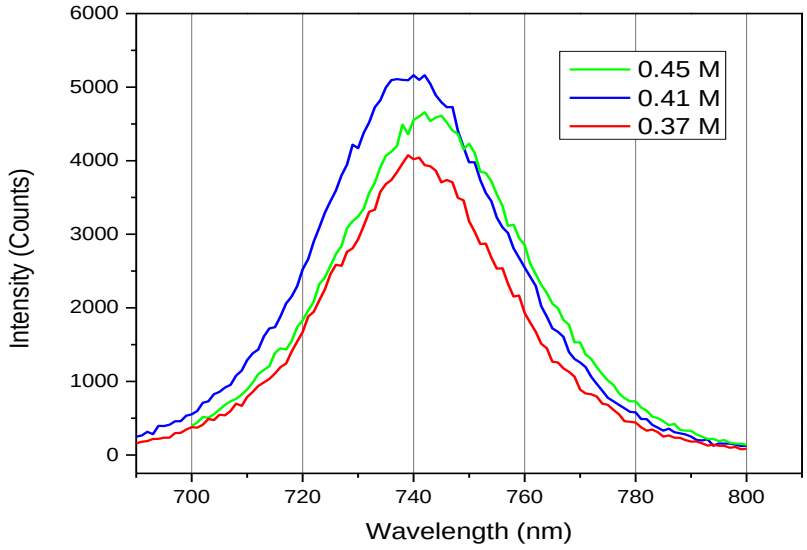

Fig 3.17: SSPL measurements of 3 samples with concentrations of 0.37, 0.41 and 0.45 M

Even though an optimized concentration of 0.41 M was found with the appropriate bandgap, the V_{oc} values were variable to a certain extent. Consequently, the V_{oc} enhancement expected after using a favorable passivation layer would not be totally apparent unless the uniformity of the V_{oc} was more uniform than the ones seen in Fig 3.15.

Our conjecture was that the PbI_2 was not getting converted completely over the entire sample area leading to this V_{oc} variability problem. Hence, one proposed mitigation solution was to reduce the thickness of the inorganic scaffold deposited during co-evaporation thus ensuring higher PbI_2 conversion although this could potentially lead to lower current densities due to thinner perovskite films. Thus, the thickness was reduced from 230 nm of PbI_2 to 200 nm and proportionately the CsBr layer deposition reduced from 23 to 20 nm.

With this new thickness, a concentration screening was again done to find the optimum concentration. A solution of 0.445 M was made and diluted to give 2 other concentrations of 0.41 and 0.37 M. The plots below in Fig 3.18 show the performance of the different samples. The V_{oc} values for both 0.41 M and 0.45 M were higher than that of 0.36 M, stabilizing around 1.12 V, while the Jsc also improved at these concentrations, with the best-performing cells reaching approximately 20 mA/cm². In contrast, the FF was highest for the 0.41 M samples, reaching up to 82%, whereas the 0.36 M samples exhibited a higher FF than 0.45 M but remained lower than 0.41 M. As a result, the PCE peaked at 17.4% for 0.41 M, establishing it as the optimized concentration.

Fig 3.19 shows the 0.41 M perovskite samples after the stipulated annealing time period. The films look uniform and have the distinct dark brown color of a perovskite film.

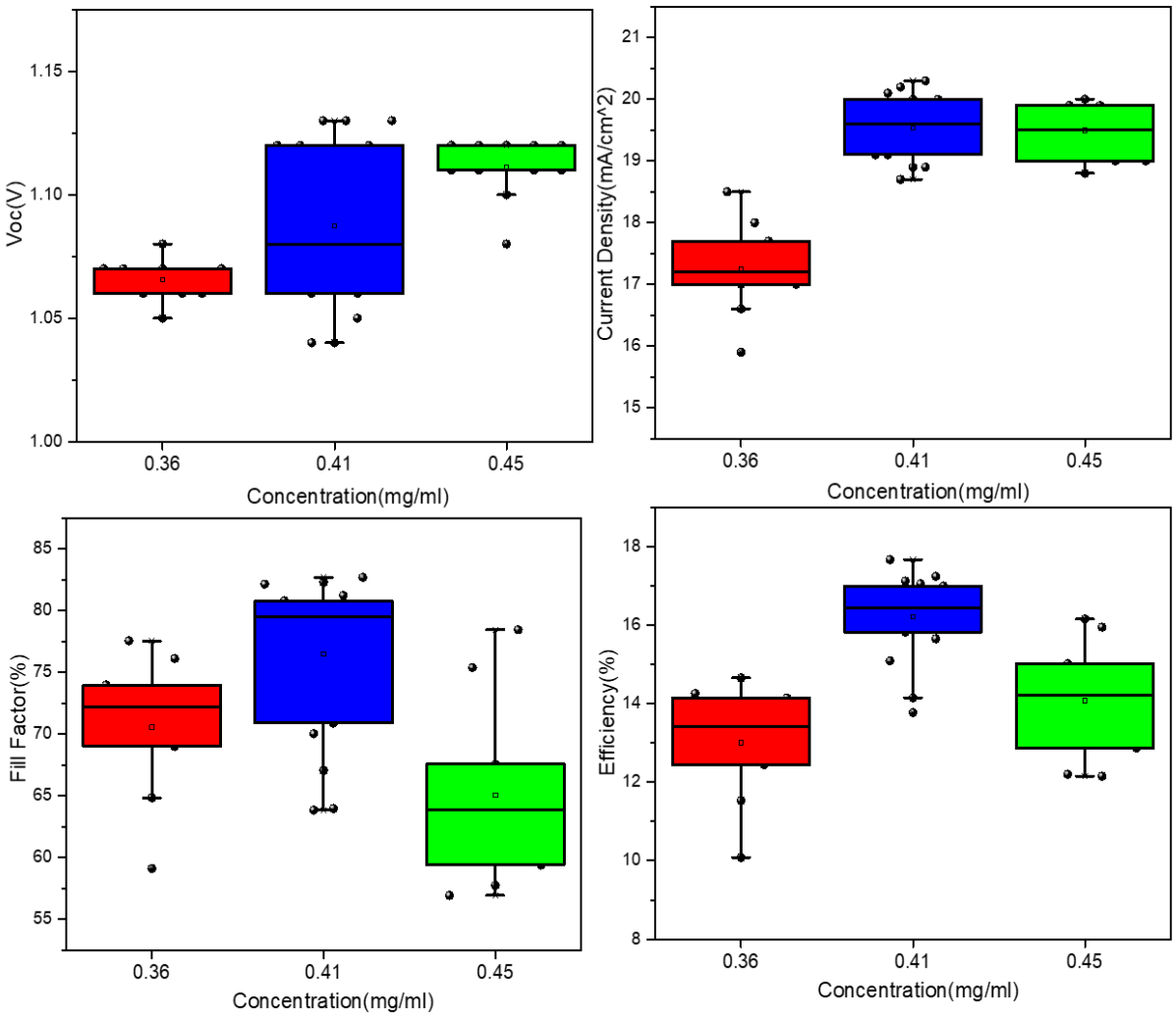

Fig 3.18: Photovoltaics parameters of the cells with organohalide concentrations at 0.36, 0.41, 0.45 M

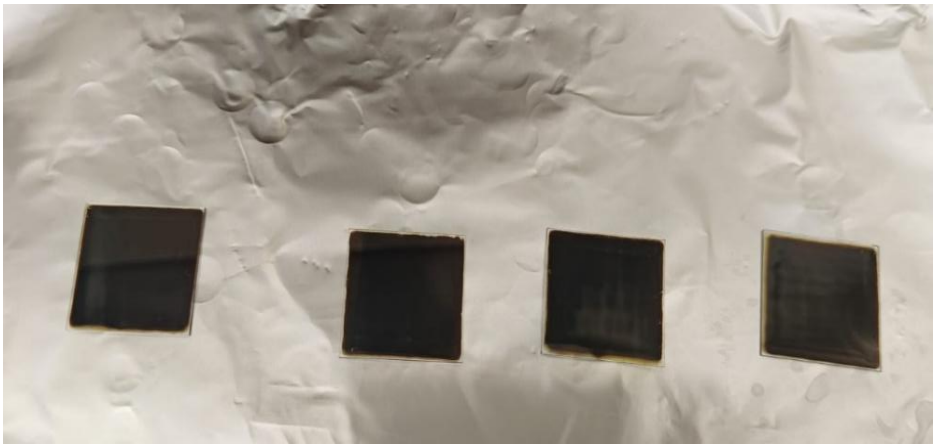

Fig 3.19: Perovskite films of 0.41 M concentration post annealing

3.3 Investigating MACl Effects

During these optimization runs, a study to observe the benefits of MACl on the perovskite film formation was also conducted. From existing literature, we know it plays a crucial role in improving the crystallization and structural quality of perovskite films while also serving as a bulk passivating agent [47]. During deposition, MACl influences the formation and arrangement of the perovskite material, leading to a more uniform and well-structured film [47]. It helps in achieving a more complete conversion of the precursor materials into the final perovskite structure, minimizing inconsistencies that can degrade device performance. Additionally, MACl interacts with the perovskite during crystallization, temporarily incorporating into the material and passivating defects within the bulk, particularly vacancies and uncoordinated sites that can act as recombination centers [47]. As MACl evaporates during annealing, it leaves behind a more ordered and defect-reduced film, resulting in better charge carrier transport and improved stability [47].

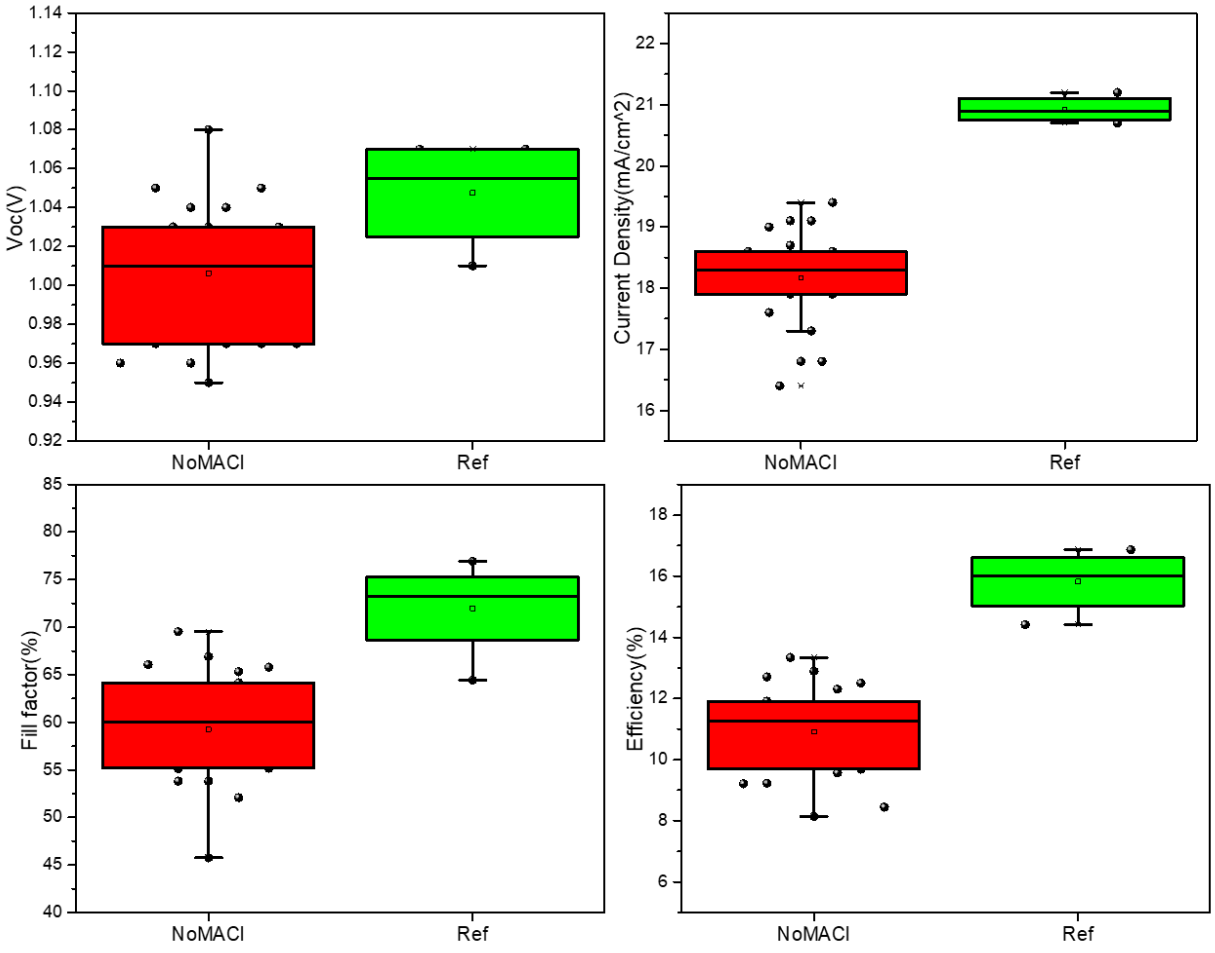

Fig 3.20: Photovoltaics parameters of the cells with and without MACl

Devices with the optimized 0.41M organohalide concentration containing 25.8% MACl were compared to those without MACl, with the performance plots shown in Fig. 3.20. A clear enhancement in all photovoltaic parameters is observed for the MACl-containing samples, leading to a significantly higher PCE.

To further investigate the impact of MACl, TRPL measurements (Fig. 3.21) were conducted, revealing a longer charge carrier lifetime for the MACl-incorporated sample. This suggests that MACl effectively passivates defect states, reducing non-radiative recombination and improving crystal quality.

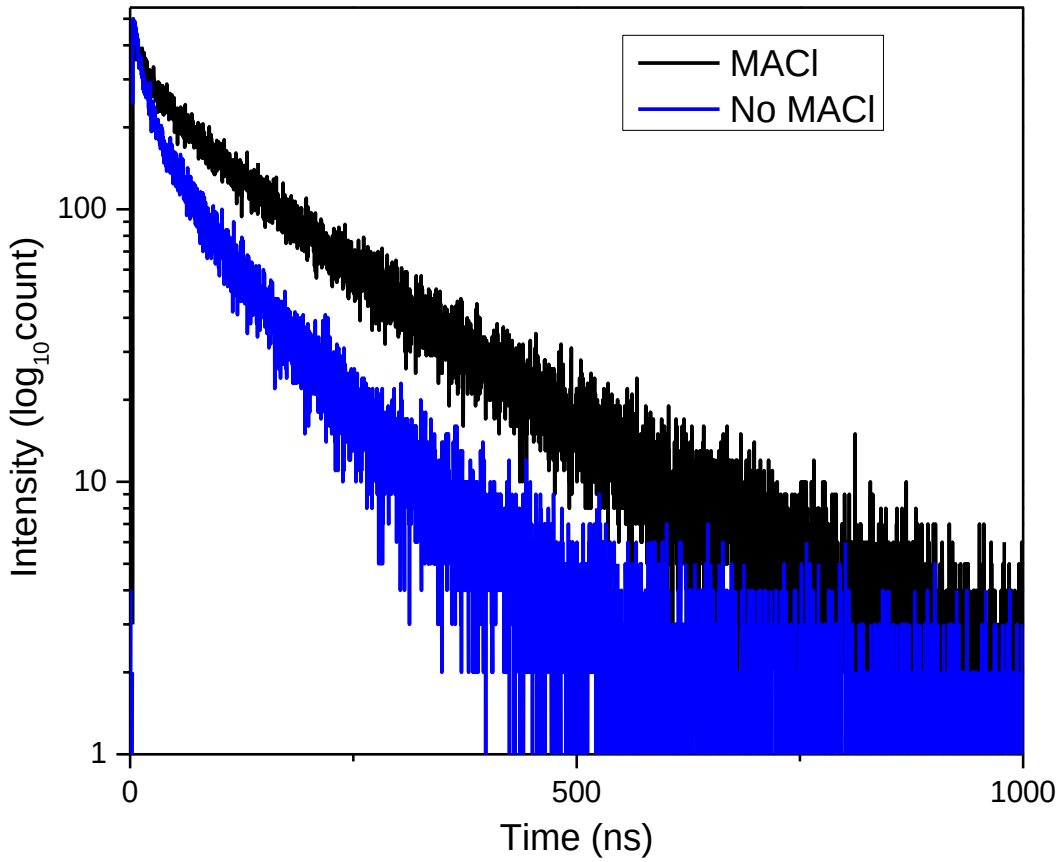

Fig 3.21: TRPL measurements of sample without and with MACl in the bulk

Additionally, SEM imaging (Fig. 3.22) highlights key morphological differences. While the non-MACl sample exhibits a few visible pinholes, which could lead to lower shunt resistance and reduced device performance, the most striking difference lies in grain size. A size distribution analysis of the samples was conducted, as shown in the distribution curves in Fig. 3.23. The non-MACl sample exhibited smaller grain sizes, with an average of 226 nm and a maximum grain size of 435 nm. In contrast, the MACl-treated sample demonstrates a significantly larger average grain size of 426 nm, with the largest grains reaching 747 nm. The increase in grain size, coupled with

fewer structural defects, reinforces the role of MACl in enhancing film uniformity, reducing grain boundary density, and ultimately improving charge transport and overall device performance.

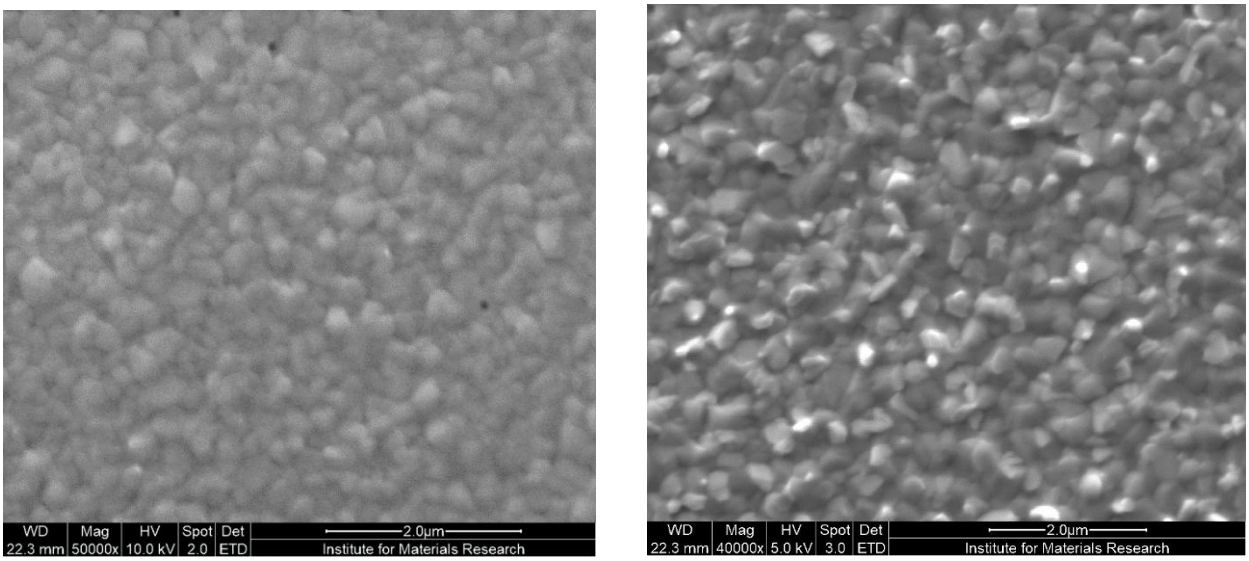

Fig 3.22: SEM images of sample without (left) and with (right) MACl

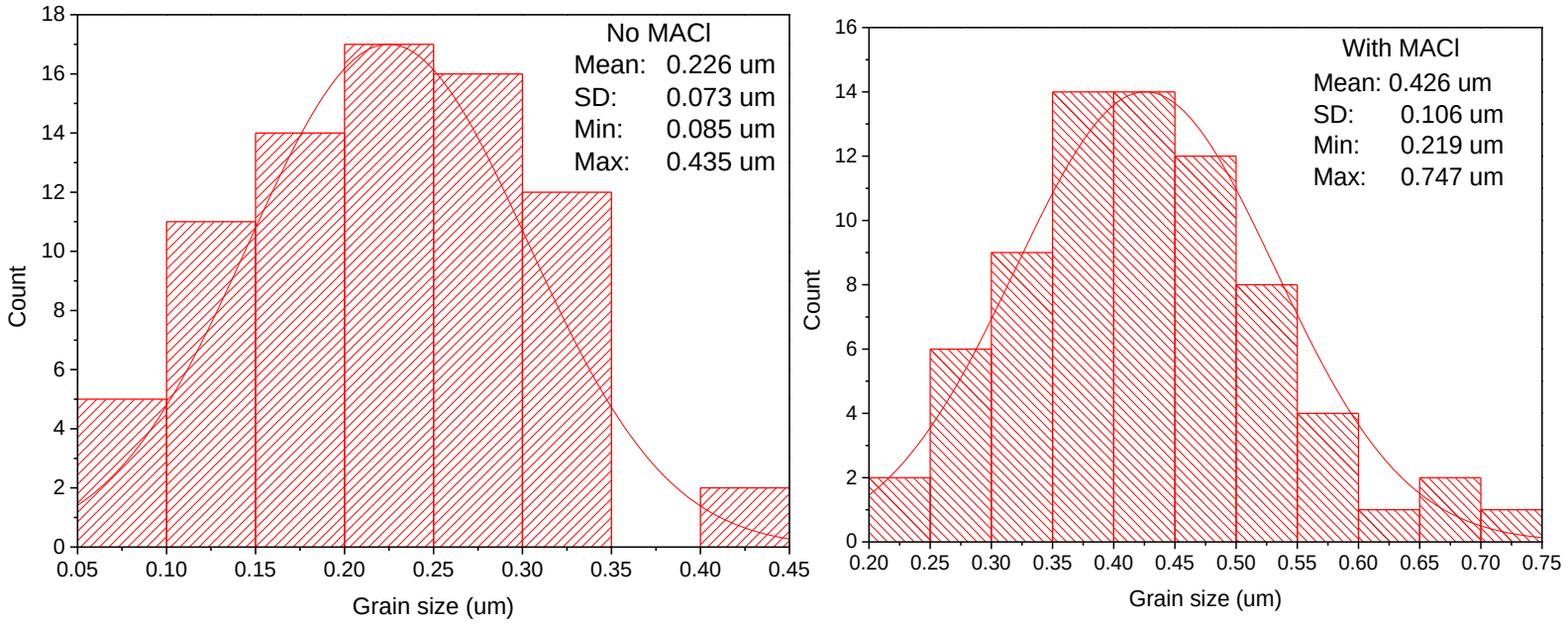

Fig 3.23: Grain size distributions of sample without (left) and with (right) MACl

3.4 Solvent Selection

With the optimized concentration established, the focus shifted toward exploring solvent modifications to assess their potential impact on device performance. To this end, isopropanol (IPA) with 1% N-Methylpyrrolidone (NMP) and 5% NMP were investigated as alternative solvents. Devices were fabricated to compare the performance of cells processed with pure IPA, IPA with 1% NMP, and IPA with 5% NMP. Additionally, SSPL and TRPL were conducted on perovskite films deposited using each solvent formulation to evaluate their effects on carrier dynamics and recombination behavior. The device performances are provided below in Fig 3.24.

Analyzing the device performance in Fig 3.24, the V_{oc} of the IPA and 1% NMP samples remain comparable, whereas the 5% NMP sample exhibits a significant drop in V_{oc}. In terms of current density, certain cells in the 1% NMP dataset outperform the IPA samples, while 5% NMP lags considerably behind. However, the FF of the IPA samples surpasses that of the 1% NMP samples, which in turn is comparable to the 5% NMP samples. As a result, the PCE of the IPA and 1% NMP samples remains similar, whereas the 5% NMP sample demonstrates significantly lower efficiency. It is worth noting that this batch of IPA-based devices exhibited slightly lower efficiency compared to previous batches, yet the observed trends remained consistent and informative.

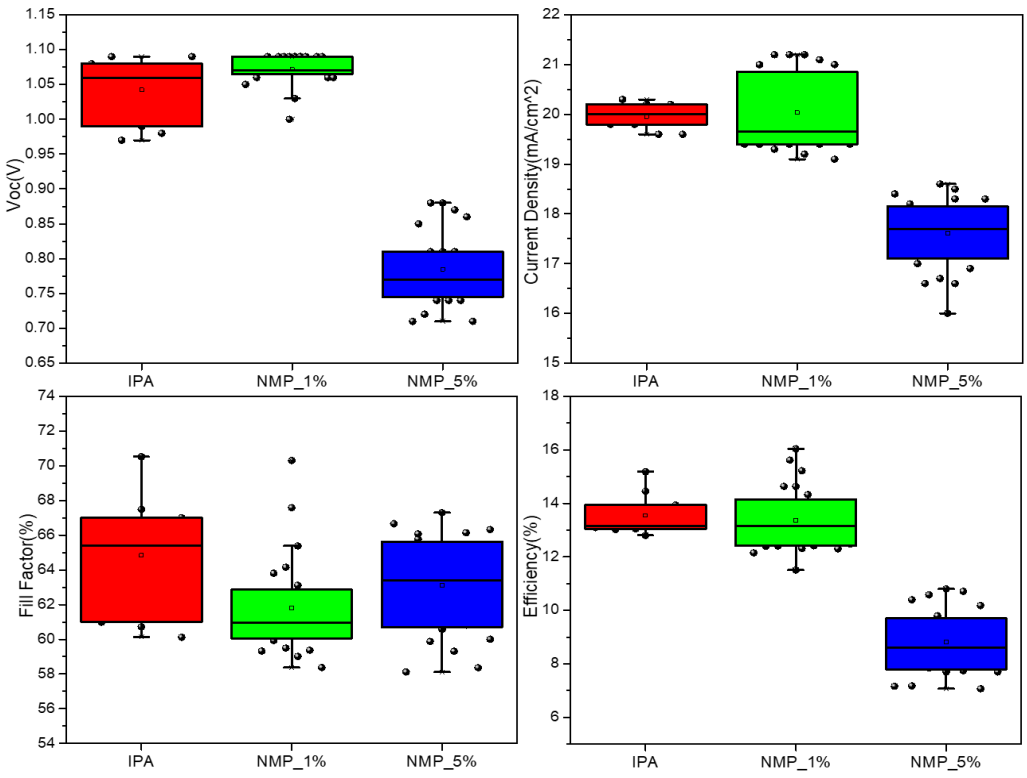

Fig 3.24: Photovoltaics parameters of the cells made with different solvent compositions

To further investigate device stability, the samples were subjected to prolonged illumination, with measurements taken at 2-minute intervals. The solid plots in Figure 3.25 represent initial measurements, while the dotted plots correspond to measurements after 10 minutes of continuous illumination. A slight V_{oc} improvement was observed across all samples. However, the current density of the 1% NMP sample dropped significantly, whereas the IPA and 5% NMP samples remained relatively stable. A similar trend was evident in the FF, with the 1% NMP sample exhibiting a pronounced decline, while the IPA and 5% NMP samples showed minimal degradation. Consequently, the PCE of the 1% NMP sample experienced a substantial decrease over time, while the IPA and 5% NMP samples maintained greater stability under illumination.

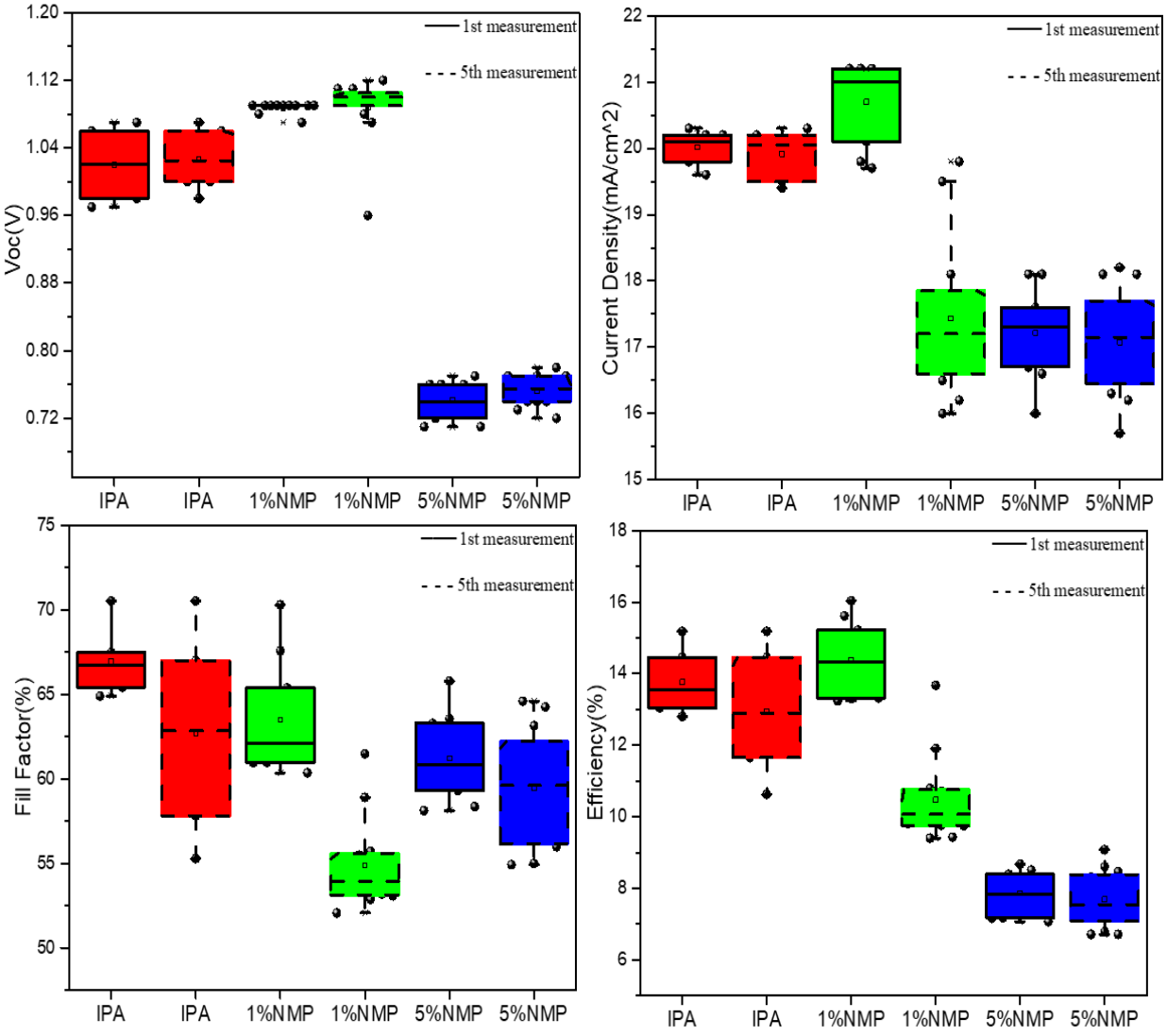

Fig 3.25: Photovoltaics parameters of cells of different solvent compositions before and after light-soaking

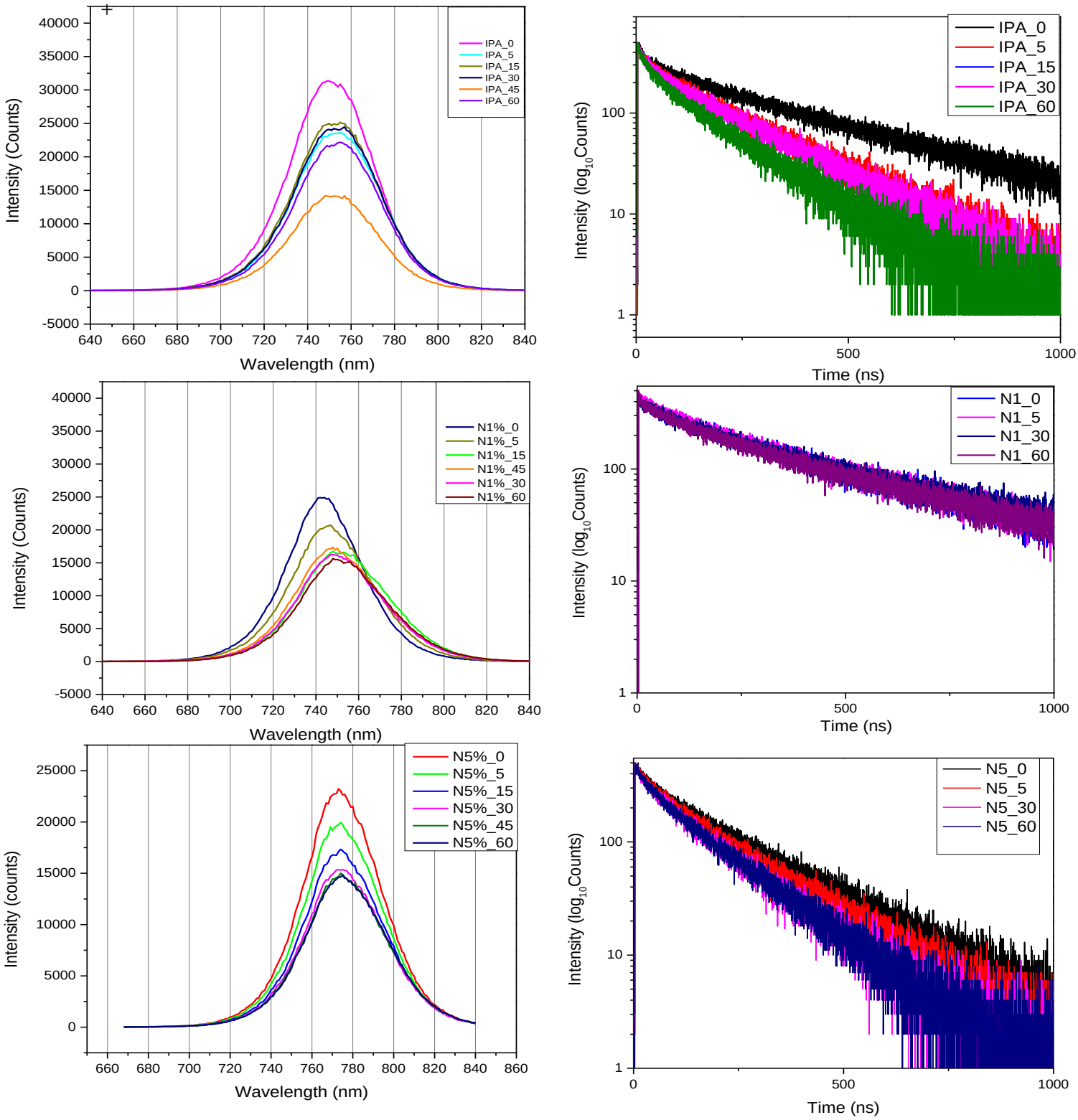

Fig 3.26: SSPL measurements (left side) of 1 spot after 0,5,15,30,45 and 60 minutes of laser illumination of samples made with IPA, IPA with 1% NMP (N1) and IPA with 5% NMP (N5) while TRPL measurements (right) of the same after 0,5,30 and 60 minutes

Films made with the different solvent compositions were put for PL measurements. SSPL measurements of a selected spot on each film were done at 0,5,15,30,45 and 60 minutes with prolonged laser illumination at their bandgap wavelength as shown in Fig 3.26 which also includes TRPL measurements of the same done after 0,5,30 and 60 minutes. The TRPL plot comparison between different solvents is displayed in Fig 3.27.

Examining the steady-state photoluminescence (SSPL) measurements, a gradual decrease in intensity was observed for all samples over time due to prolonged laser exposure. Among them, the IPA sample exhibited the highest initial intensity, suggesting superior crystal quality. Additionally, no PL peak shift was detected even after one hour of laser illumination, indicating a relatively stable composition with a consistent bandgap around 746 nm. In contrast, the 1% NMP sample initially exhibited a PL peak at 742 nm, but a progressive redshift was observed with continued illumination, ultimately reaching 750 nm after 60 minutes. This shift in emission wavelength suggests halide segregation within the crystal structure, likely due to ion migration under prolonged illumination. The 5% NMP sample, however, displayed the lowest initial PL intensity, indicative of poor film quality. Furthermore, its initial bandgap of 765 nm (1.62 eV) deviated significantly from the target 1.67 eV, reinforcing that higher NMP concentrations negatively impact perovskite film formation and lead to suboptimal optoelectronic properties.

The time-resolved photoluminescence (TRPL) measurements revealed distinct carrier lifetime behaviors across the samples. The 1% NMP sample initially exhibited the highest carrier lifetime among the three samples (as shown in Fig 3.27) and remained relatively stable even after one hour of continuous illumination (Fig 3.26), suggesting better defect passivation and reduced non-radiative recombination over time. In contrast, the IPA sample, which had a slightly lower charge carrier lifetime than 1% NMP (as shown in Fig 3.27) showed a noticeable decline in carrier lifetime within the first five minutes, after which it stabilized (as can be seen in Fig 3.26). This rapid initial drop may indicate the presence of trap states or defect activation under illumination, leading to increased non-radiative recombination. However, the subsequent stabilization suggests that the film quality remained largely intact beyond the initial degradation phase. The 5% NMP sample, on the other hand, exhibited a consistently low carrier lifetime from the beginning (Fig 3.27), with no significant change over time (Fig 3.26). This indicates poor initial film quality, likely due to excessive NMP disrupting perovskite crystallization and increasing defect density, resulting in a high rate of charge carrier recombination.

EQE measurements were performed on the best-performing devices, namely the IPA and 1% NMP samples, as shown in Fig 3.27. The 1% NMP sample exhibited a higher EQE% across the measured wavelength range, which is consistent with its higher initial current density compared to the IPA sample, as seen in the device performance plots. Additionally, small spikes observed in the EQE spectra for both samples can be attributed to artifacts from the calibration procedure which uses a silicon reference cell, leading to minor overestimations of EQE% at specific

wavelengths. However, this does not affect the overall trend and relative comparison between the samples.

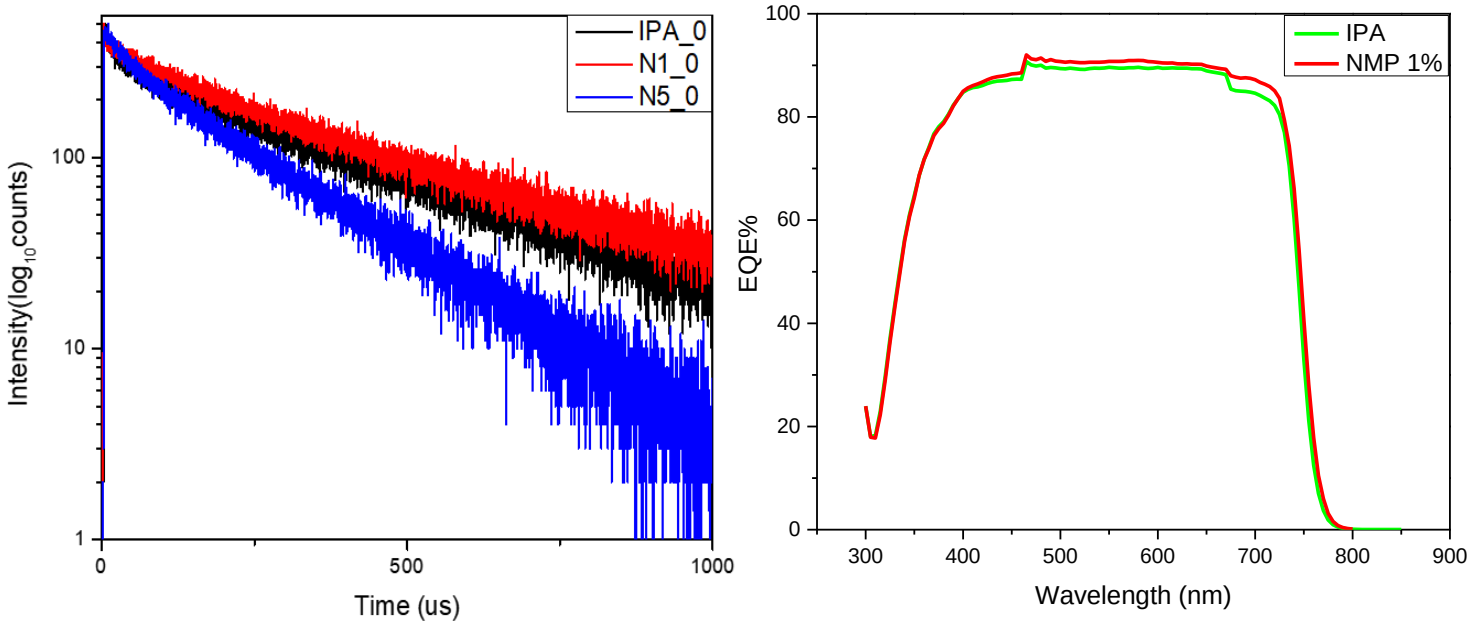

Fig 3.27: On left, comparison of initial TRPL measurements of IPA, IPA with NMP 1% and IPA with NMP 5% samples and on right, EQE Plots of IPA vs NMP 1%

3.5 Blade-coated perovskite surface passivation

Having covered all bases to optimize the reference recipe, the focus shifted towards enhancing the performance of the cells by using a surface passivation layer. The blade-coating speed was kept fixed at 5 mm/s. As done during spin-coating, after depositing the passivation layer annealing was done inside the glovebox at 100°C for 5 minutes followed by the subsequent steps of ETL deposition and so on. Due to the paucity of time, only PDAI2 was tested for perovskite surface passivation with the observations and results presented in the following pages.

3.5.1 Surface Passivation with PDAI2

Having worked with $PDAI_2$ before during spin-coating and knowing how widely used it is in contemporary literature, this was the material chosen for perovskite surface defects passivation.

A preliminary concentration optimization was conducted using 1 mg/ml, 0.75 mg/ml, 0.5 mg/ml, and 0.25 mg/ml of $PDAI_2$, with the corresponding performance plots presented in Figure 3.28. A

notable enhancement in V_{oc} was observed for all passivated samples compared to the reference; however, the 0.5 mg/ml samples exhibited slightly lower V_{oc} values than the other three concentrations. In terms of current density, the 0.25 mg/ml, 0.75 mg/ml, and 1 mg/ml passivated samples exhibited a significant reduction compared to the reference, whereas the 0.5 mg/ml sample maintained a Jsc comparable to the reference, further highlighting its anomalous behavior. Additionally, the FF was lower across all passivated samples relative to the reference, with the 0.5 mg/ml sample displaying the highest FF among the passivated variants. Consequently, PCE of all passivated samples remained below the reference, although certain 0.5 mg/ml cells yielded PCE values comparable to the reference.

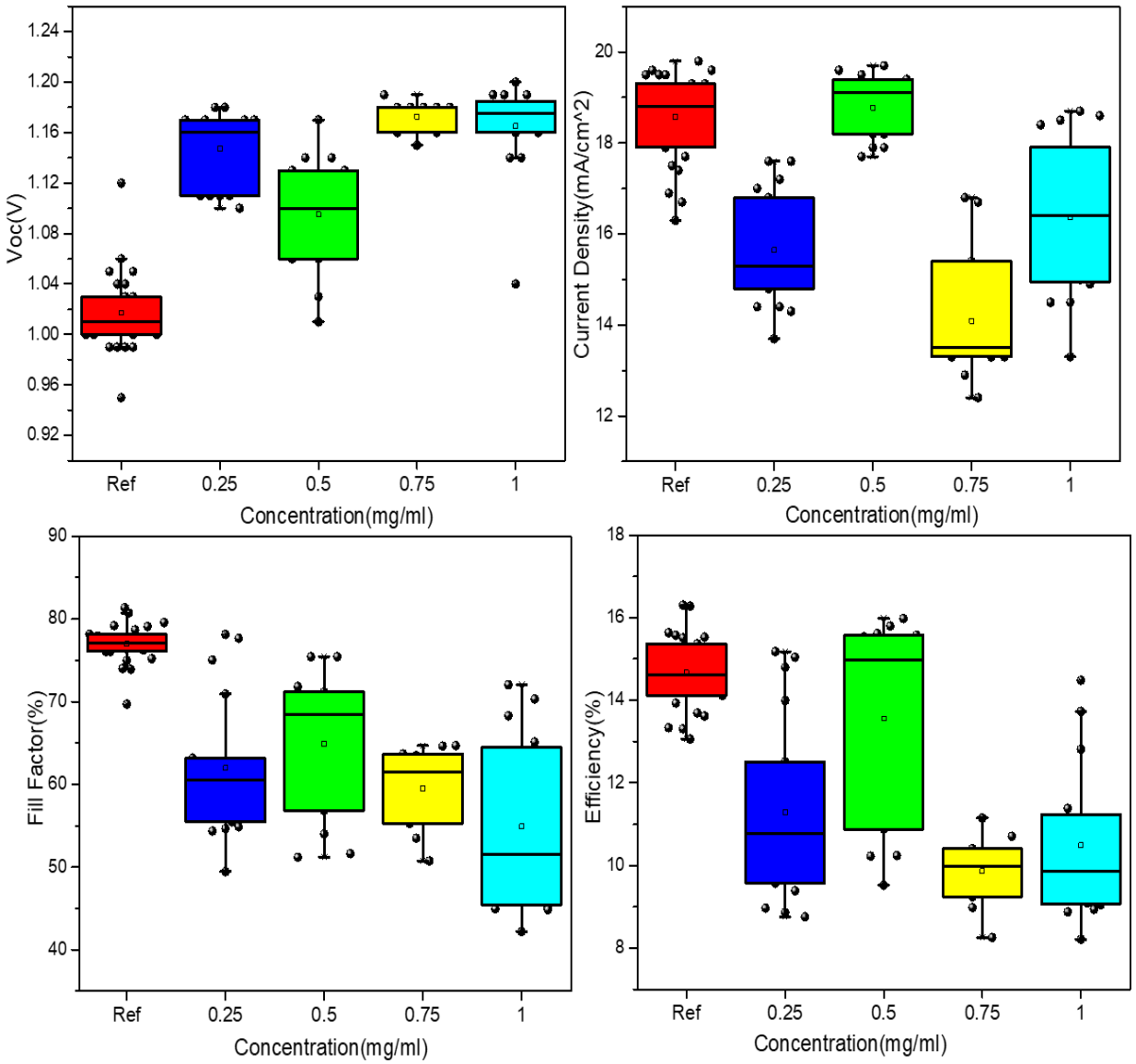

Fig 3.28: Performance parameters of samples without (Ref) and with $PDAI_2$ as a surface passivation layer at concentrations of 0.25, 0.5, 0.75 and 1 mg/ml

Our conjecture for these trends is that the $PDAI_2$ layer is excessively thick, leading to the formation of an insulating barrier that hinders charge transport. This increased resistance results in a reduction in Jsc and FF, ultimately degrading device performance. On the contrary, an optimal $PDAI_2$ concentration should ideally enhance interfacial properties without introducing significant resistive losses that impede charge transport. Based on these observations, one might assume that the optimal $PDAI_2$ concentration lies near 0.5 mg/ml. However, if this assumption were correct, the 0.25 mg/ml sample should not exhibit V_{oc} enhancement and FF reduction, as a lower concentration would behave similar to the reference. Another issue was the lower V_{oc} enhancement observed for the 0.5 mg/ml sample compared to the 0.25 mg/ml sample, suggesting that the passivation layer deposition for 0.5 mg/ml may have encountered processing inconsistencies. Given all these points, the behavior of the 0.5 mg/ml sample can likely be attributed to coating-related issues, and its data implications can be safely disregarded when drawing conclusions about the optimal concentration. Hence, the major implication from these trends was to either move towards lower concentrations of $PDAI_2$ or try rinsing after the passivation step.

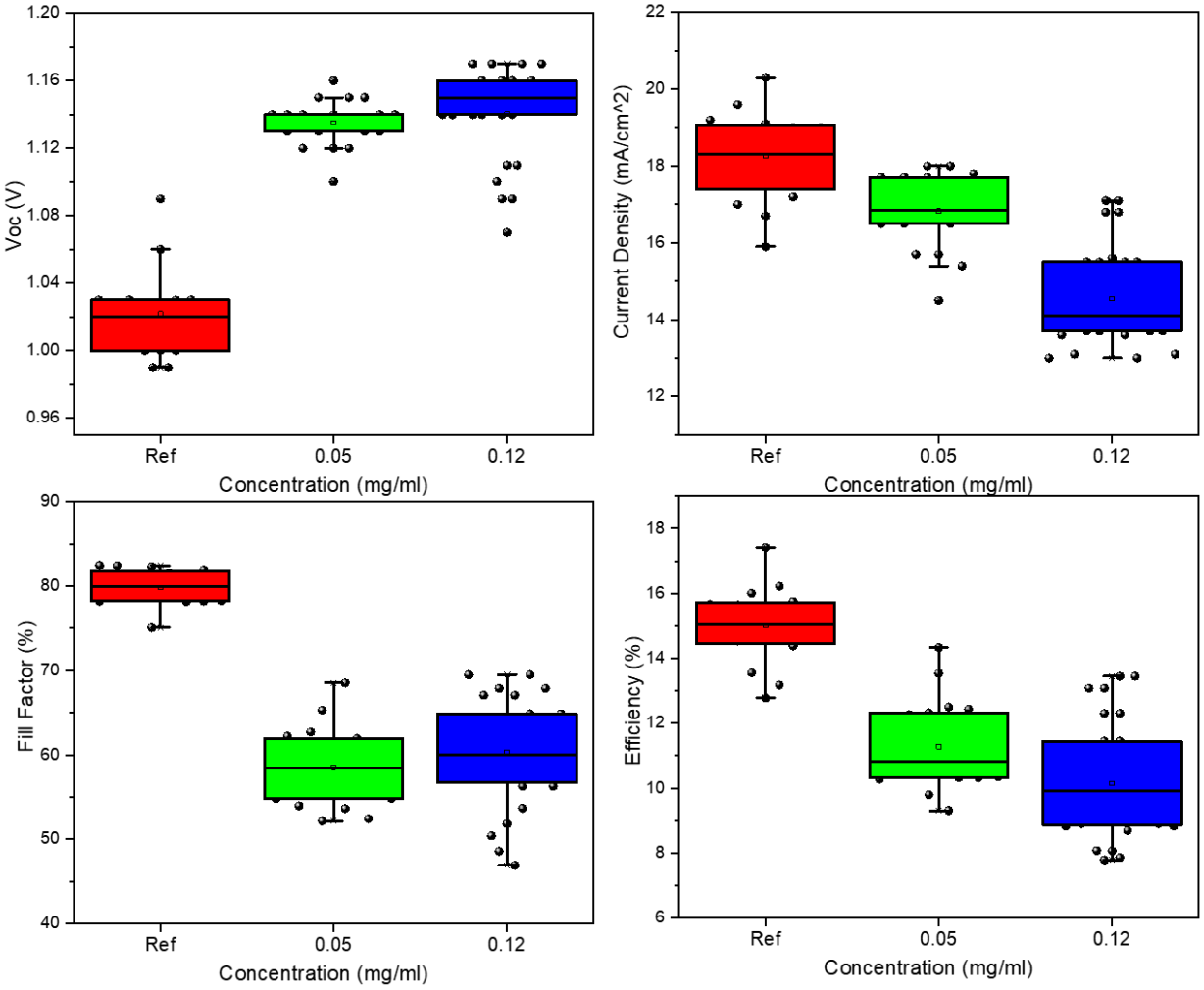

Fig 3.29: Performance parameters of samples without (Ref) and with $PDAI_2$ as a surface passivation layer at concentrations of 0.05 and 0.12 mg/ml

Lower concentrations of 0.05 mg/ml and 0.12 mg/ml of $PDAI_2$ were thus tested, with their performance plots shown in Fig. 3.29. The results follow a similar trend to the higher concentrations, exhibiting a notable enhancement in V_{oc}, particularly for 0.12 mg/ml, which surpasses the 0.5 mg/ml sample in this regard. However, both concentrations show a decline in current density and FF, with the 0.12 mg/ml sample experiencing a more pronounced drop. Consequently, these losses in Jsc and FF result in a lower overall PCE for both concentrations compared to the reference device.

An attempt with even lower concentrations was carried out with 0.01 and 0.005 mg/ml, with the corresponding performance plots shown in Fig. 3.30. While some cells within each sample exhibited a slight V_{oc} improvement, others displayed V_{oc} values similar to the reference, suggesting inconsistent passivation across the film. The current density remained largely comparable to the reference for most devices, while the FF for the 0.01 mg/ml sample was similar to the reference. In contrast, some cells in the 0.005 mg/ml sample showed a noticeable FF decline, likely indicating the presence of $PDAI_2$ at certain regions. As a result, the overall efficiency remained comparable to the reference. These observations suggest that at such low concentrations, $PDAI_2$ coverage may be highly uneven, leading to inconsistent passivation effects. Given this, the alternative approach—rinsing—was adopted to assess whether any improvements in performance can be made.

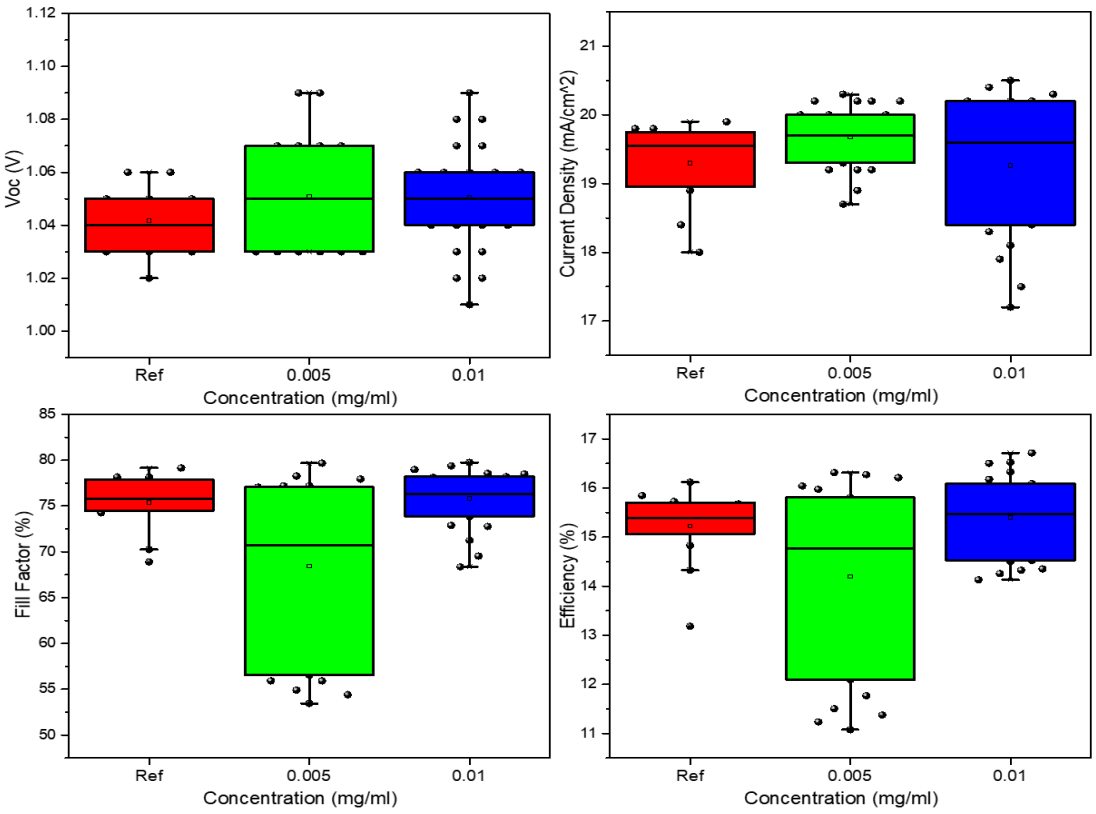

Fig 3.30: Performance parameters of samples without (Ref) and with $PDAI_2$ as a surface passivation layer at concentrations of 0.005 and 0.01 mg/ml

Given the previous results, the alternative approach—rinsing—was adopted to assess whether any improvements in performance can be made. Samples coated with 0.25 mg/ml $PDAI_2$ were put for rinsing to observe whether it could help wash away some $PDAI_2$ aggregates or help these passivating molecules to reach other defect spots in the crystal. The rinsing process was done by spin-coating IPA onto the surface passivated samples at 3000 rpm for 30 seconds followed by 2 minutes of annealing. These were compared against untreated references and samples with 0.25 mg/ml $PDAI_2$ deposited onto but not rinsed. The results of the same are shown below in Fig 3.31.

Both the rinsed and non-rinsed $PDAI_2$-treated samples exhibited a V_{oc} enhancement of approximately 20-30 mV compared to the reference. However, the current density for both passivated samples remained lower than the reference value, indicating potential limitations in charge transport. The FF of the rinsed samples showed an improvement over the non-rinsed counterparts, suggesting that rinsing may have helped reduce resistive losses or improve interface quality. Nevertheless, the FF remained lower than that of the reference, which itself was slightly lower than values observed in other batches. As a result, while rinsing led to better overall performance compared to the non-rinsed sample, the efficiency still fell short of the reference device, highlighting the need for further optimization of the passivation process.

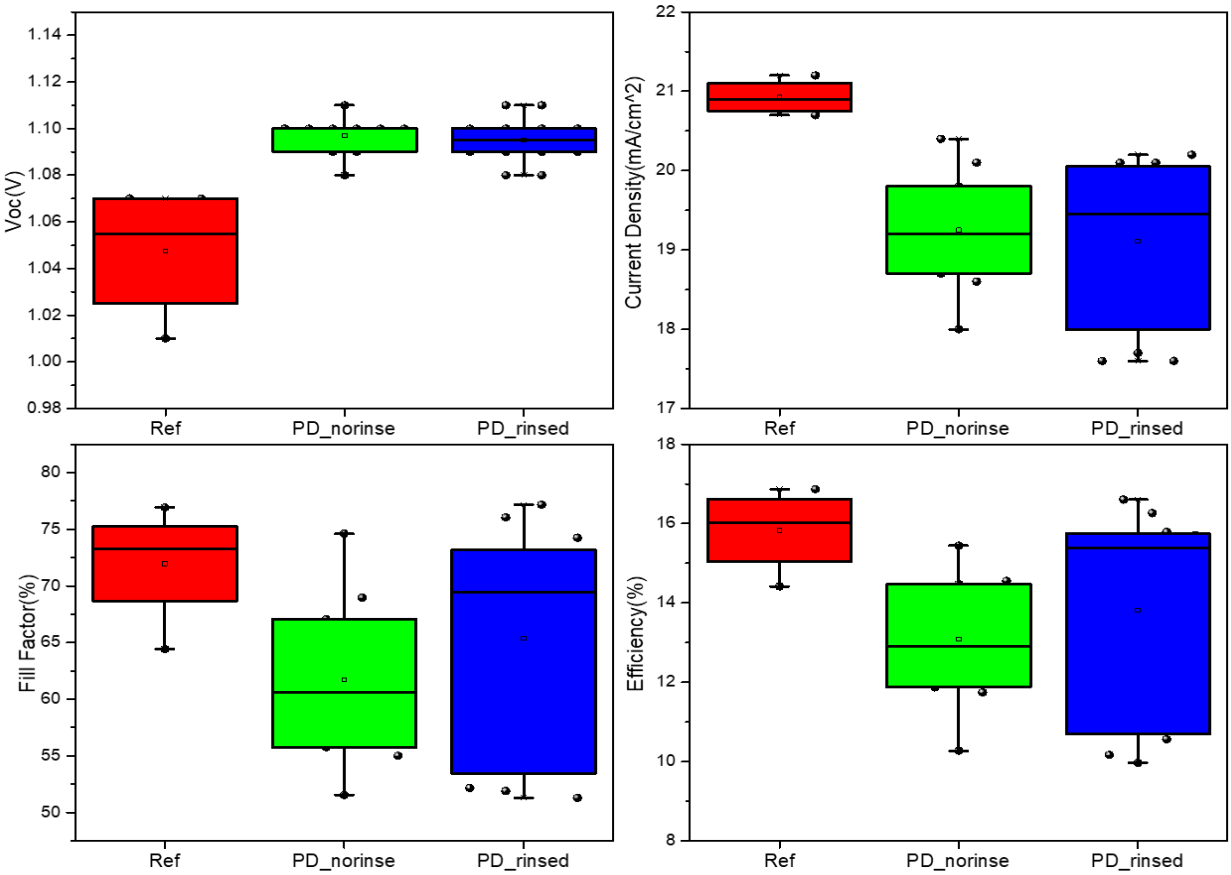

Fig 3.31: Performance Parameters of 0.25 mg/ml concentration $PDAI_2$ passivated samples with and without rinsing compared against Reference (Ref)

Additionally, TRPL measurements and SEM imaging were conducted on the reference, non-rinsed, and rinsed perovskite films to further investigate the impact of $PDAI_2$ treatment.

As shown in Fig. 3.32, the non-rinsed $PDAI_2$ sample exhibited a slight improvement in charge carrier lifetime, while the rinsed sample demonstrated a more significant enhancement, suggesting that rinsing may have helped improve defect passivation and reduce non-radiative recombination pathways.

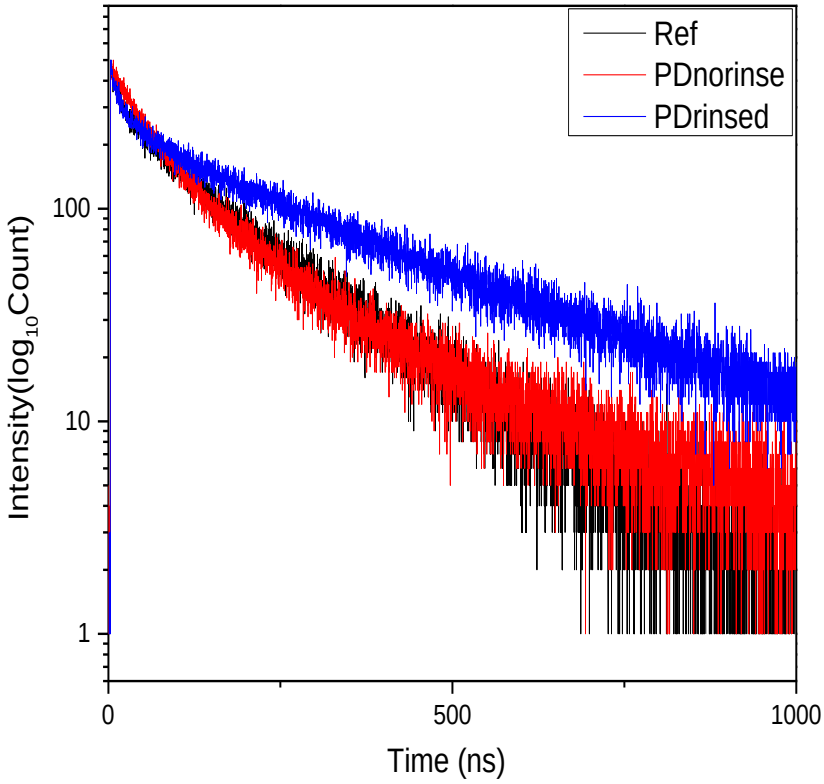

Fig 3.32: TRPL Measurement of $PDAI_2$ passivated samples with and without rinsing compared against reference

The SEM images of the non-rinsed and rinsed samples, shown in Fig. 3.33, exhibit similar film features, indicating that the grain size remains consistent with the pre-passivated perovskite film. This suggests that $PDAI_2$ does not negatively impact film morphology or induce significant structural changes.

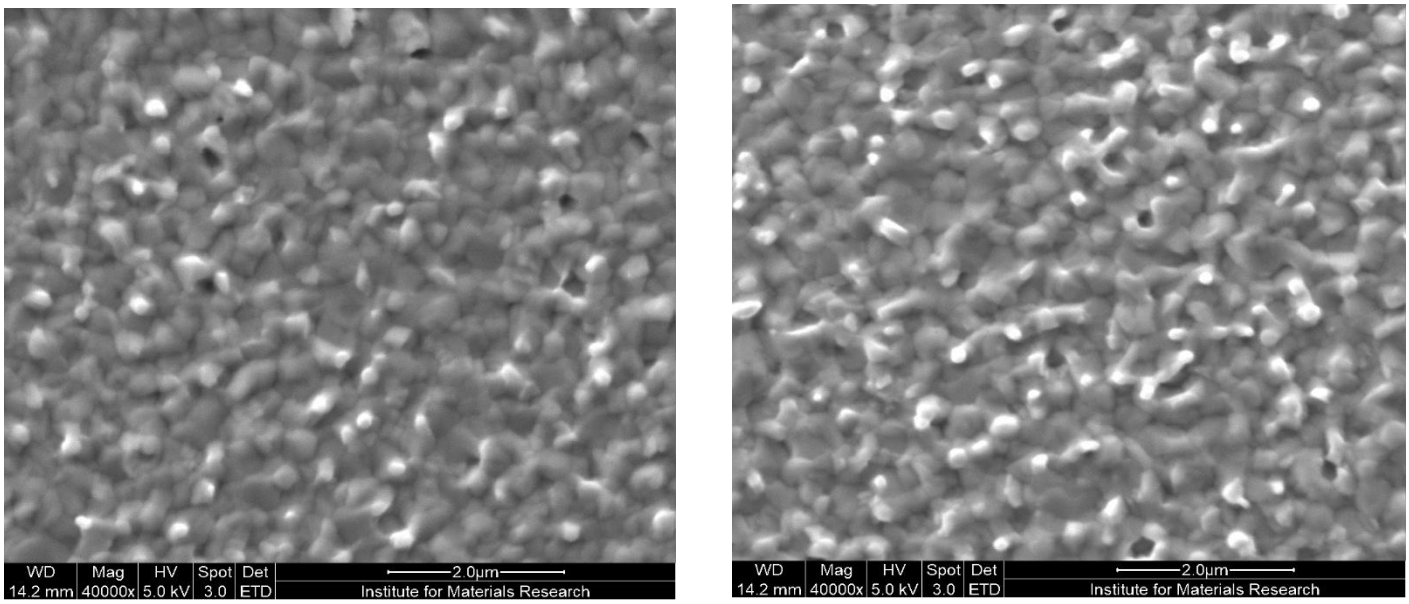

Fig 3.33: SEM images of $PDAI_2$ treated sample without (left) and followed by rinsing(right)

Chapter 4: Conclusions and Outlook

The development of high-efficiency, stable, and scalable perovskite solar cells remains a crucial step toward the commercialization of perovskite-silicon tandem photovoltaics. This thesis focused on optimizing the performance of 1.67 eV wide-bandgap perovskite solar cells by investigating bulk and surface passivation strategies and transitioning from spin-coating to blade-coating for more scalable deposition. The key findings from this work provide important insights into defect passivation, film quality control, and deposition reproducibility, all of which are essential for industrial-scale integration.

Initially, spin-coating was used for depositing the precursor organohalide solution and passivation additives to explore both bulk and surface modifications of the perovskite layer. These passivation strategies showed promising improvements in V_{oc}, though there remains significant room for further optimization.

Pentafluorobenzyl phosphonic acid (pFBPA) as a bulk additive led to a slight V_{oc} improvement at 100 µg/mL, while Jsc and FF remained comparable to the reference when the PbI_2:CsBr evaporation ratio was 2:0.6. Under continuous light soaking however, V_{oc} increased, but both pFBPA-treated samples showed a decline in Jsc and overall efficiency, suggesting stability concerns. With the transition from the 2:0.6 to the optimized 1:0.1 PbI_2:CsBr co-evaporation ratio, Jsc and FF improved, but the expected V_{oc} enhancement remained minimal. Further characterization techniques, such as Deep-Level Transient Spectroscopy (DLTS), can provide deeper insight into defect density, trap states, and their reduction post-passivation.

In terms of surface passivation, pFBPA, Piperazinium Iodide (PI), and Propane-1,3-Diammonium Iodide ($PDAI_2$) were investigated. While $PDAI_2$ led to performance degradation at the tested concentrations, pFBPA and PI demonstrated certain improvements, particularly when followed by a rinsing step in the case of PI. Advanced characterization techniques such as DLTS and Kelvin Probe Force Microscopy (KPFM) could further analyze changes in surface potential and defect density, providing a more detailed understanding of the passivation effects.

However, batch-to-batch variability in spin-coated devices introduced reproducibility challenges, making it difficult to draw definitive conclusions. This variability highlighted the need for a more controlled deposition method, and with scalability in mind, the transition to blade-coating was introduced earlier than initially planned.

In blade-coating, the perovskite precursor concentration was optimized to 0.41 M, with the champion cell achieving an efficiency of 17.4%. Additionally, to maintain the 1.67 eV bandgap, the organohalide concentration ratio was adjusted, ensuring bandgap consistency.

MACl, which had been included in the precursor during spin-coating, was further explored under blade-coating. The study, incorporating JV data, SSPL, TRPL measurements, and SEM imaging, demonstrated that MACl usage led to improved crystallinity, enlarged grain size, and effective defect passivation, resulting in longer charge carrier lifetimes. Interestingly, SEM imaging also revealed another distinct morphological difference between the MACl and non-MACl treated films, as shown in Fig. 4.1. In the MACl-containing films, two distinct crystal formations were observed, which were absent in the non-MACl samples. To further analyze the structural composition and phase distribution, an X-Ray Diffraction (XRD) analysis of the samples is necessary.

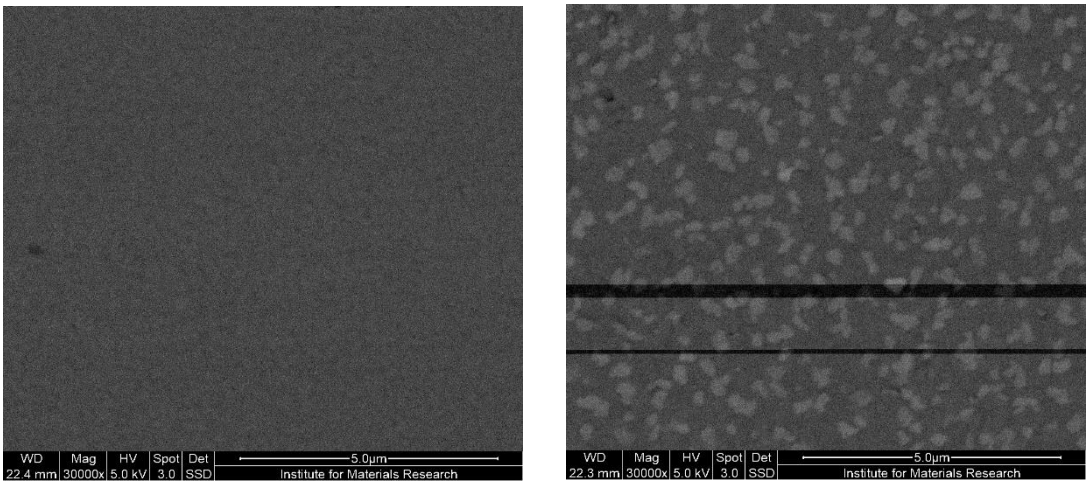

Fig 4.1: Perovskite films without (left) and with (right) MACl

To refine blade-coating, solvent engineering was conducted by comparing isopropanol (IPA) with N-methylpyrrolidone (NMP) additions. 1% NMP initially improved device performance, but prolonged illumination studies revealed ion migration effects and bandgap shifts, raising concerns about long-term stability.

Finally, $PDAI_2$ was revisited for blade-coated surface passivation, but higher concentrations led to insulating effects, while lower concentrations showed inconsistent coverage. Introducing rinsing as a post-deposition step partially mitigated these challenges, suggesting a potential pathway for further improvements in passivation techniques. Interestingly, the density of those crystalline features found in the MACl treated perovskite film (Fig 4.1) decreased upon $PDAI_2$

passivation (0.25 mg/ml). It was further reduced when passivation was followed by rinsing as can be seen in Fig 4.2.

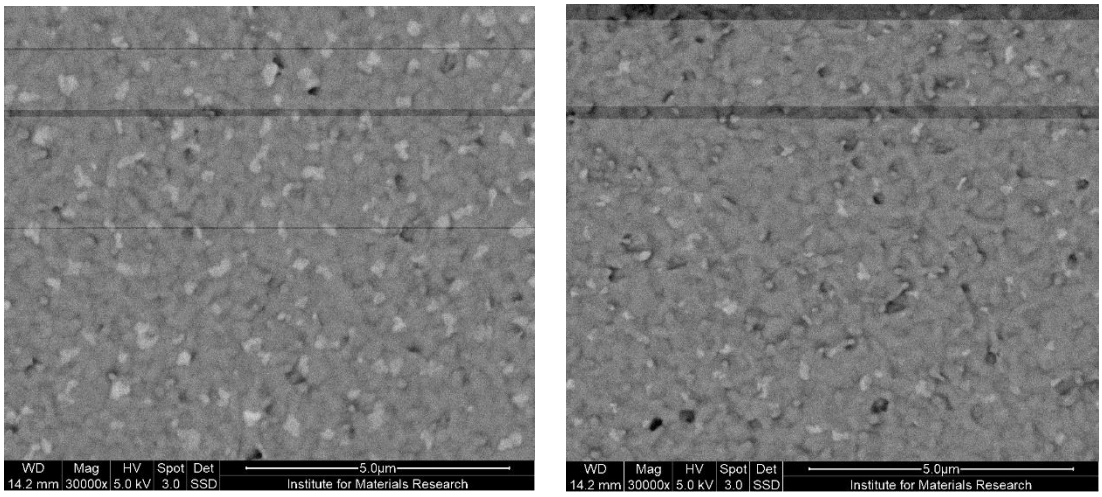

Fig 4.2: $PDAI_2$ treated perovskite films without (left) and with (right) rinsing

Also, a close look at the SEM images in Fig. 3.32 reveal a higher count of 'bright spots' for the rinsed sample than the non-rinsed one. A starker contrast can be noticed below in Fig. 4.3. To further investigate these features, X-Ray Diffraction (XRD) analysis should be conducted to provide insight into their structural characteristics. Moreover, future research on passivation strategies could benefit from real-time in situ monitoring techniques to track the crystallization process, enabling better control over film formation and defect passivation.

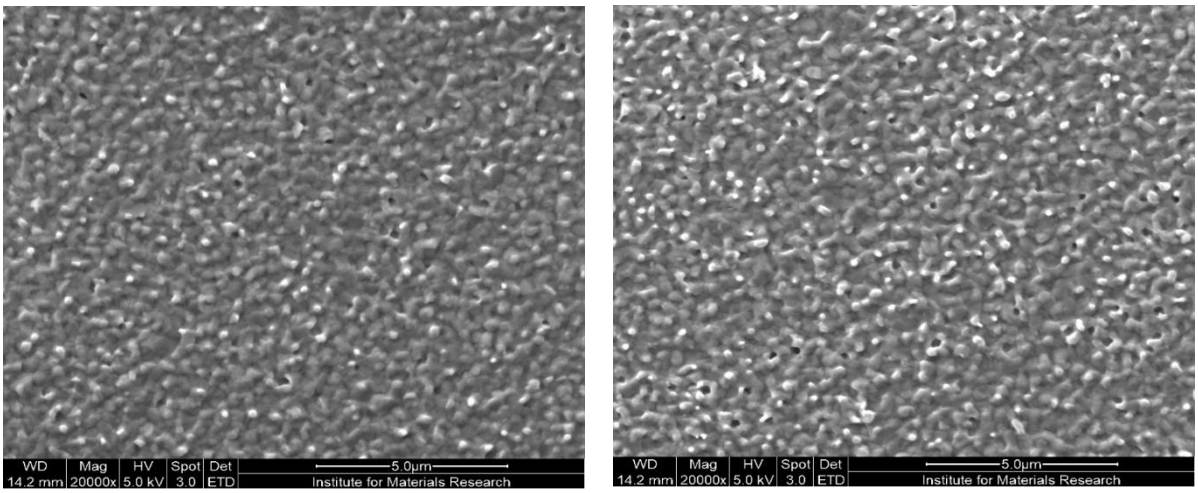

Fig 4.3: SEM images of $PDAI_2$ treated perovskite films without(left) and with (right) rinsing

Importantly, using Quasi-Fermi Level Splitting (QFLS) studies to assess the electronic quality of perovskite layers and identifying non-radiative recombination losses would help provide better understanding and would be crucial for translating the results from single-junction solar cells to high efficiency perovskite/silicon tandem solar cells.

ACKNOWLEDGEMENTS

I sincerely acknowledge the scholarship from KU Leuven which supported my project stay. I am grateful to the entire EnergyVille lab community for their help and support throughout this journey. A special thank you to my mentor, Cristian, for his guidance in processing techniques, and to Yinghuan for the insightful discussions that helped me progress.

Heartfelt thanks to my Kot 119 friends—Ide, Marie, Méron, Ysia, Alp, and Emma—for their support and bringing joy during the most challenging moments. Lastly, I am deeply grateful to my friends in India for staying connected and keeping me motivated throughout this project.

Bibliography:

1. IRENA (2023), Renewable energy statistics 2023, International Renewable Energy Agency, AbuDhabi https://www.irena.org/media/Files/IRENA/Agency/Publication/2023/Jul/IRENARenewable_energy_statistics_2023.pdf

2. IEA (2024), World Energy Outlook 2024, IEA, Paris https://www.iea.org/reports/world-energy-outlook-2024, Licence: CC BY 4.0 (report); CC BY NC SA 4.0 (Annex A)

3. Tandem Photovoltaics – From the Laboratory into the World - Fraunhofer ISE. (n.d.). Fraunhofer Institute for Solar Energy Systems ISE. https://www.ise.fraunhofer.de/en/key-topics/tandem-photovoltaics.html

4. Solar Cell Structure | PVEDucation. (n.d.). https://www.pveducation.org/pvcdrom/solar-cell-operation/solar-cell-structure

5. Open-Circuit Voltage | PVEDucation. (n.d.). https://www.pveducation.org/pvcdrom/solar-cell-operation/open-circuit-voltage

6. Short-Circuit current | PVEDucation. (n.d.). https://www.pveducation.org/pvcdrom/solar-cell-operation/short-circuit-current

7. IV Curve | PVEDucation. (n.d.). https://www.pveducation.org/pvcdrom/solar-cell-operation/iv-curve

8. Fill Factor | PVEDucation. (n.d.). https://www.pveducation.org/pvcdrom/solar-cell-operation/fill-factor

9. Solar Cell Efficiency | PVEDucation. (n.d.). https://www.pveducation.org/pvcdrom/solar-cell-operation/solar-cell-efficiency

10. Shockley, W. and Queisser, H.J. (1961) Detailed Balance Limit of Efficiency of P-N Junction Solar Cells. Journal of Applied Physics, 32, 510-519

11. Baiju, A., & Yarema, M. (2022). Status and challenges of multi-junction solar cell technology. Frontiers in Energy Research, 10. https://doi.org/10.3389/fenrg.2022.971918

12. Department of Materials Science and Metallurgy - University of Cambridge. (n.d.). Direct and indirect band gap semiconductors

13. Best Research-Cell Efficiency Chart. (n.d.). Photovoltaic Research | NREL. https://www.nrel.gov/pv/cell-efficiency.html

14. ScienceDirect. Perovskite. https://www.sciencedirect.com/topics/ earth-and-planetary-sciences/perovskite: Fig 1.5

15. Suleiman Bello, Adam Urwick, Francesco Bastianini, Alisyn J. Nedoma, Alan Dunbar, August 2022; An introduction to perovskites for solar cells and their characterisation

16. Yao Tong, Adel Najar, Le Wang, Lu Liu, Minyong Du, Jing Yang, Jianxun Li, Kai Wang,*and Shengzhong (Frank) Liu, Science 2022; Wide-Bandgap Organic–Inorganic Lead Halide Perovskite Solar Cells, https://doi.org/10.1002/advs.202105085

17. Zhang, T., Dar, M. I., Li, G., Xu, F., Guo, N., Grätzel, M., & Zhao, Y. (2017). Bication lead iodide 2D perovskite component to stabilize inorganic α-CsPbI 3 perovskite phase for high-efficiency solar cells. Science Advances, 3(9). https://doi.org/10.1126/sciadv.1700841

18. Hoke, E. T., Slotcavage, D. J., Dohner, E. R., Bowring, A. R., Karunadasa, H. I., & McGehee, M. D. (2014). Reversible photo-induced trap formation in mixed-halide hybrid perovskites for photovoltaics. Chemical Science, 6(1), 613–617. https://doi.org/10.1039/c4sc03141e

19. Lee, J., Kim, D., Kim, H., Seo, S., Cho, S. M., & Park, N. (2015). Formamidinium and cesium hybridization for Photo- and Moisture-Stable perovskite solar cell. Advanced Energy Materials, 5(20). https://doi.org/10.1002/aenm.201501310

20. McMeekin, D. P., Sadoughi, G., Rehman, W., Eperon, G. E., Saliba, M., Hörantner, M. T., Haghighirad, A., Sakai, N., Korte, L., Rech, B., Johnston, M. B., Herz, L. M., & Snaith, H. J. (2016). A mixed-cation lead mixed-halide perovskite absorber for tandem solar cells. Science, 351(6269), 151–155. https://doi.org/10.1126/science.aad5845

21. Bush, K. A., Frohna, K., Prasanna, R., Beal, R. E., Leijtens, T., Swifter, S. A., & McGehee, M. D. (2018). Compositional Engineering for Efficient Wide Band Gap Perovskites with Improved Stability to Photoinduced Phase Segregation. ACS Energy Letters, 3(2), 428–435. https://doi.org/10.1021/acsenergylett.7b01255

22. Al-Ashouri, A., Köhnen, E., Li, B., Magomedov, A., Hempel, H., Caprioglio, P., Márquez, J. A., Vilches, A. B. M., Kasparavicius, E., Smith, J. A., Phung, N., Menzel, D., Grischek, M., Kegelmann, L., Skroblin, D., Gollwitzer, C., Malinauskas, T., Jošt, M., Matič, G., . . . Albrecht, S.

(2020). Monolithic perovskite/silicon tandem solar cell with >29% efficiency by enhanced hole extraction. Science, 370(6522), 1300–1309. https://doi.org/10.1126/science.abd4016

23. Al-Ashouri, A., Magomedov, A., Roß, M., Jošt, M., Talaikis, M., Chistiakova, G., Bertram, T., Márquez, J. A., Köhnen, E., Kasparavičius, E., Levcenco, S., Gil-Escrig, L., Hages, C. J., Schlatmann, R., Rech, B., Malinauskas, T., Unold, T., Kaufmann, C. A., Korte, L., . . . Albrecht, S. (2019). Conformal monolayer contacts with lossless interfaces for perovskite single junction and monolithic tandem solar cells. Energy & Environmental Science, 12(11), 3356–3369. https://doi.org/10.1039/c9ee02268f

24. Chen, H., Liu, C., Xu, J., Maxwell, A., Zhou, W., Yang, Y., Zhou, Q., Bati, A. S. R., Wan, H., Wang, Z., Zeng, L., Wang, J., Serles, P., Liu, Y., Teale, S., Liu, Y., Saidaminov, M. I., Li, M., Rolston, N., . . . Sargent, E. H. (2024). Improved charge extraction in inverted perovskite solar cells with dual-site-binding ligands. Science, 384(6692), 189–193. https://doi.org/10.1126/science.adm9474

25. Jiang, Q., Tirawat, R., Kerner, R. A., Gaulding, E. A., Xian, Y., Wang, X., Newkirk, J. M., Yan, Y., Berry, J. J., & Zhu, K. (2023). Towards linking lab and field lifetimes of perovskite solar cells. Nature, 623(7986), 313–318. https://doi.org/10.1038/s41586-023-06610-7

26. He, R., Wang, W., Yi, Z., Lang, F., Chen, C., Luo, J., Zhu, J., Thiesbrummel, J., Shah, S., Wei, K., Luo, Y., Wang, C., Lai, H., Huang, H., Zhou, J., Zou, B., Yin, X., Ren, S., Hao, X., . . . Zhao, D. (2023). Improving interface quality for 1-cm2 all-perovskite tandem solar cells. Nature, 618(7963), 80–86. https://doi.org/10.1038/s41586-023-05992-y

27. Li, Z., Sun, X., Zheng, X., Li, B., Gao, D., Zhang, S., Wu, X., Li, S., Gong, J., Luther, J. M., Li, Z., & Zhu, Z. (2023). Stabilized hole-selective layer for high-performance inverted p-i-n perovskite solar cells. Science, 382(6668), 284–289. https://doi.org/10.1126/science.ade9637

31. Jiang, Q., & Zhu, K. (2024). Rapid advances enabling high-performance inverted perovskite solar cells. Nature Reviews Materials, 9(6), 399–419. https://doi.org/10.1038/s41578-024-00678-x

32. Bae, S., Heo, D., & Kim, S. (2022). Recent progress of perovskite devices fabricated using thermal evaporation method: Perspective and outlook. Materials Today Advances, 14, 100232. https://doi.org/10.1016/j.mtadv.2022.100232

33. Hamukwaya, S. L., Hao, H., Zhao, Z., Dong, J., Zhong, T., Xing, J., Hao, L., & Mashingaidze, M. M. (2022). A review of recent developments in preparation methods for Large-Area Perovskite solar cells. Coatings, 12(2), 252. https://doi.org/10.3390/coatings12020252

34. Niu, X., Li, N., Chen, Q., & Zhou, H. (2020). Insights into Large-Scale Fabrication Methods in Perovskite Photovoltaics. Advanced Energy and Sustainability Research, 2(2). https://doi.org/10.1002/aesr.202000046

35. MENSAH, S. Y. & UNIVERSITY OF CAPE COAST, GHANA. (n.d.). SOLAR CELL AND ITSAPPLICATIONhttps://indico.cern.ch/event/145296/contributions/1381075/attachments/136874/194161/Presentation_at_KNUST.pdf

36. Photoluminescence spectroscopy. (n.d.). Photovoltaic Research | NREL. https://www.nrel.gov/pv/photoluminescence-spectroscopy.html

37. Scanning Electron Microscopy Blog Archives | Nanoscience Instruments. (n.d.). Nanoscience Instruments https://www.nanoscience.com/tech/scanning-electron-microscopy/

38. Mokobi, F. (2024, May 25). Scanning Electron Microscope (SEM): Principle, parts, uses - Microbe notes. Microbe Notes. https://microbenotes.com/scanning-electron-microscope-sem/

39. Chin, X. Y., Turkay, D., Steele, J. A., Tabean, S., Eswara, S., Mensi, M., Fiala, P., Wolff, C. M., Paracchino, A., Artuk, K., Jacobs, D., Guesnay, Q., Sahli, F., Andreatta, G., Boccard, M., Jeangros, Q., & Ballif, C. (2023). Interface passivation for 31.25%-efficient perovskite/silicon tandem solar cells. Science, 381(6653), 59–63. https://doi.org/10.1126/science.adg0091

40. Turkay, D., Artuk, K., Chin, X., Jacobs, D. A., Moon, S., Walter, A., Mensi, M., Andreatta, G., Blondiaux, N., Lai, H., Fu, F., Boccard, M., Jeangros, Q., Wolff, C. M., & Ballif, C. (2024). Synergetic substrate and additive engineering for over 30%-efficient perovskite-Si tandem solar cells. Joule, 8(6), 1735–1753. https://doi.org/10.1016/j.joule.2024.04.015

41. Mariotti, S., Köhnen, E., Scheler, F., Sveinbjörnsson, K., Zimmermann, L., Piot, M., Yang, F., Li, B., Warby, J., Musiienko, A., Menzel, D., Lang, F., Keßler, S., Levine, I., Mantione, D., Al-Ashouri, A., Härtel, M. S., Xu, K., Cruz, A., . . . Albrecht, S. (2023). Interface engineering for high-performance, triple-halide perovskite–silicon tandem solar cells. Science, 381(6653), 63–69. https://doi.org/10.1126/science.adf5872

42. Liu, C., Yang, Y., Chen, H., Xu, J., Liu, A., Bati, A. S. R., Zhu, H., Grater, L., Hadke, S. S., Huang, C., Sangwan, V. K., Cai, T., Shin, D., Chen, L. X., Hersam, M. C., Mirkin, C. A., Chen, B., Kanatzidis, M. G., & Sargent, E. H. (2023). Bimolecularly passivated interface enables

efficient and stable inverted perovskite solar cells. Science, 382(6672), 810–815. https://doi.org/10.1126/science.adk1633

43. Heydarian, M., Heydarian, M., Schygulla, P., Reichmuth, S. K., Bett, A. J., Hohl-Ebinger, J., Schindler, F., Hermle, M., Schubert, M. C., Schulze, P. S. C., Borchert, J., & Glunz, S. W. (2023). Recent progress in monolithic two-terminal perovskite-based triple-junction solar cells. Energy & Environmental Science, 17(5), 1781–1818. https://doi.org/10.1039/d3ee02822d

44. Ghazal, H., & Sohail, N. (2022). Sputtering deposition. In IntechOpen eBooks. https://doi.org/10.5772/intechopen.107353

45. Er-Raji, O., Rustam, L., Kore, B. P., Glunz, S. W., & Schulze, P. S. C. (2023). Insights into Perovskite Film Formation Using the Hybrid Evaporation/Spin-Coating Route: An In Situ XRD Study. ACS Applied Energy Materials, 6(11), 6183–6193. https://doi.org/10.1021/acsaem.3c00698

46. Substrate colour change in spin coater. (n.d.-c). [Video]. Ossila. https://www.ossila.com/pages/spin-coating

47. Wang, C., He, B., Fu, M., Su, Z., Zhang, L., Zhang, J., Mei, B., & Gao, X. (2024). Influence of MACL on the crystallization kinetics of perovskite via a Two-Step Method. Crystals, 14(5), 399. https://doi.org/10.3390/cryst14050399